Title

A Hybrid Positron Emission Tomography Imaging Modality: Combining Gamma and Positron Imaging



Author

Shoop, Greyson

Publication Date

2023

Peer reviewed|Thesis/dissertation

UNIVERSITY OF CALIFORNIA
SANTA CRUZ

# A HYBRID POSITRON EMISSION TOMOGRAPHY IMAGING MODALITY: COMBINING GAMMA AND POSITRON IMAGING

A thesis submitted in partial satisfaction of the
requirements for the degree of

MASTER OF SCIENCE

in

SCIENTIFIC COMPUTING & APPLIED MATHEMATICS

by

**Greyson Shoop**

December 2023

The Thesis of Greyson Shoop
is approved:

Professor Marcella Gomez, Chair

Professor Shiva Abbaszadeh

Professor Hongyun Wang

Professor François Monard

Peter Biehl
Vice Provost and Dean of Graduate Studies

# Table of Contents

# List of Figures

# List of Tables

# List of Symbols & Abbreviations

## Symbols

| | |
|---|---|
| $*$ | Convolution operator |
| $\beta$ | Unit vector in direction of Compton cone axis |
| $\beta^+$ | High energy positron emitted from radioactive decay |
| $\beta^-$ | High energy electron emitted from radioactive decay |
| $\gamma$ | Photons originating from nuclear decay processes |
| $\in$ | Element of, or, belongs to |
| $\lambda_j$ | Activity in voxel $j$ |
| $\mathbb{R}^n$ | Real coordinate space of dimension $n$ |
| $\mathbb{Z}^{0+}$ | Set of non-negative integers |
| $\mathbf{R}^{\#}$ | Radon transform adjoint operator |
| $\mathbf{R}f$ | Radon transform of a function $f$ |
| $\mathcal{C}(u, \beta, \theta)$ | Set of Compton cone surfaces with parameters $u, \beta, \theta$ |
| $\mathcal{L}$ | Likelihood function |

| | |
|---|---|
| $\mathfrak{B}f$ | Back-projection operator on $f$ |
| $\mu(\cdot)$ | Attenuation function of $(\cdot)$ |
| $\mu_i$ | Expected mean number of photons detected in bin $i$ |
| $\notin$ | Does not belong to, or is not a member of |
| $\phi$ | Polar scattering angle of recoil electron in Compton scattering |
| $\prod$ | Product of a sequence of values |
| $e^+$ | Positron |
| $e^-$ | Electron |
| n | Neutron |
| $p^+$ | Proton |
| $\theta$ | Polar scattering angle of a Compton scattered photon and the half-open angle of a Compton cone |
| $\times$ | Cartesian product. Set of all ordered pairs. |
| $\arg\max_{\lambda}(\cdot)$ | Value of $\lambda$ that maximimizes $(\cdot)$ |
| $d\Omega$ | Differential angular range of Compton scattered photons at a scattering angle $\theta$ |
| $d\sigma$ | Differential-cross section of interaction of incoming Compton scattered photons |
| $E(\cdot)$ | Expectation of $(\cdot)$ |
| $E_i$ | Incident or incoming photon energy |

| | |
|---|---|
| $E_s$ | Energy carried by a Compton scattered photon |
| $M$ | Set of coordinates defined within detector geometry |
| $P_1$ | Compton scattering event containing position and energy data |
| $P_2$ | Photoelectric absorption event containing position and energy data |
| $S^n$ | Space of $n$-dimension unit sphere |
| $t_{1/2}$ | Half-life of an isotope |
| $t_{ij}$ | System matrix with probability that detected cone $i$ originated from voxel $j$ |
| $u$ | Location of vertex of Compton cone |
| $v$ | Neutrino |
| $X_{ij}$ | Poisson random variable for the number of photons emitted by voxel $j$ contributing to bin $i$ |
| $Y_i$ | Poisson random variable for the total number of photons detected in bin $i$ |
| Z | Number of protons in an atom |

# Abreviations

| | |
|---|---|
| FDG | 2-deoxy-2[$^{18}$F]fluoro-D-Glucose |
| PA | Positron Annihilation |
| LOR | Line of Response |
| TOF-PET | Time of Flight PET |

| | |
|---|---|
| SPECT | Single Photon Emission Computed Tomography |
| DCSc | Double Compton Scattering |
| COR | Cone of Response |
| $^{44}$Sc | Scandium-44 |
| $^{68}$Ga | Gallium-68 |
| $^{72}$As | Arsenic-72 |
| PET | Positron Emission Tomography |
| $^{89}$Zr | Zirconium-89 |
| $^{124}$Iodine | Iodine-124 |
| PSMA | Prostate Specific Membrane Antigen |
| J-PET | Jagiellonian PET |
| LM | List-Mode |
| GPU | Graphics Processing Unit |
| CUDA | Compute Unified Device Architecture |
| FWHM | Full Width at Half Maximum |
| FOV | Field of View |
| MLEM | Maximum Likelihood Expectation Maximization |
| RHS | Right Hand Side |
| CC | Compton Camera |

| | |
|---|---|
| CZT | Cadmium Zinc Telluride |
| GATE | GEANT4 Application for Tomographic Emission |
| ECT | Emission Computed Tomography |
| $^{177}$Lu | Lutetium-177 |
| CT | Computed Tomography |
| $^{18}$F | Flourine-18 |

**Abstract**

A Hybrid Positron Emission Tomography Imaging Modality: Combining Gamma and Positron Imaging

by

Greyson Shoop

Utilizing prompt gamma emissions in radionuclides has potential to enable new opportunities in Positron Emission Tomography (PET). The Compton scattering and imaging of the prompt gamma-ray provide extra information that aid in correcting for positron range error and as a consequence, enable an improved system sensitivity and image quality. In addition, by coincidence windowing the 511 keV positron annihilation photons and the prompt-gamma, it is possible to differentiate between multiple PET tracers since in many nuclides, prompt gammas are emitted with energy unique to the nuclide and are emitted almost simultaneously at the time of decay before positron annihilation can occur. In this study, we explore this concept through a simulation study. In order to demonstrate the feasibility of imaging prompt-gamma emitting radionuclides combined with PET, we implement a Maximum-Likelihood Expectation Maximization (MLEM) image reconstruction algorithm for Compton Camera (CC) imaging on an existing dual-panel Cadmium Zinc Telluride (CZT) PET system simulated by a Monte Carlo based simulation toolkit GEANT4 Application for Tomographic Emission (GATE). The CZT detector is a good candidate for a hybrid imaging modality because of its large cross-section for Compton scattering at high energy, its good energy resolution ($> 5$ % full width half maximum at 511 keV), and a wide dynamic range to measure energy from 100 keV to 1.2 MeV.

# Acknowledgments

I'd like to acknowledge professor Shiva Abbaszadeh in providing me with invaluable opportunities to work in her lab and challenge myself. I could not have done any of this without her support and advice.

I would like to acknowledge and thank Kimia Gholami and Gregory Romancheck for providing python processing for providing PET coincidence data for use in PET image reconstruction. Additionally I owe much of my knowledge of GATE and image reconstruction to Gregory and thank him for taking the time to help me understand and work with my results.

Lastly I must thank everyone apart of Radiological Instrumentations Laboratory here at UC Santa Cruz for being amazing team players and working with each other to perform to the best of our abilities.

# Chapter 1

# Introduction

The number of Positron Emission Tomography (PET) scans increase each year and is becoming more widely used due to its versatility as a non-invasive functional imaging tool, meaning that we can image and visualize metabolic processes within patients without having to physically incise a patient [1]. With applications in oncology for diagnosing various cancers such as prostate cancer, lymphoma, carcinoma and cardiac hypoxia as well as the emerging field of *theranostics* (imaging informed/guided radiotherapy), the field is moving fast with the need for innovations in improving nuclear medical imaging systems [2] [3]. Among the challenges that face modern Emission Computed Tomography (ECT) systems such as PET are the need for sub-millimeter resolutions for correctly localizing tumor cells for accurate diagnoses. For example, the $\beta^-$ particles emitted from Lutetium-177 ($^{177}$Lu) that are used to kill cancerous cells in prostate cancer treatment have soft-tissue penetration of about 670 $\mu$m [4] [5] [6]. Exceptional image resolution is therefore important so that physicians can accurately quantify how much radiation they are exposing their patient to and most importantly where. This is the motivation behind developing systems that are capable of imaging a variety of radiotracers and detecting emissions that are radiotracer unique. The work

we present aims to demonstrate the capabilities of a *edge-on* Cadmium Zinc Telluride (CZT) dual-panel dedicated head and neck PET system for operation as a hybrid imaging system utilizing both PET and Compton Camera (CC) imaging modalities.

We begin with this introductory section where we discuss fundamental medical imaging physics. This work takes place in the context of a large multidisciplinary field of medical imaging and ECT. Therefore the fundamental physical processes of PET and CC imaging technologies must be properly presented in order to understand the the challenges present in nuclear medical imaging. We begin by introducing and discussing the basics of PET and CC imaging. We then present recent challenges that researchers the field are taking on and discuss how these problems are being faced in the form of hybrid imaging modalities. We then propose the implementation of CC Imaging on an existing dual-panel CZT dedicated head and neck PET system in order to improve system sensitivity.

In Chapter 2 we will introduce the Radon transform in the context of X-Ray CT and present its extrapolation to PET and CC imaging. We discuss the basics of forward projection and back-projection which are concepts implemented in modern statistical iterative reconstruction techniques. We then conclude by formulating the Maximum Likelihood Expectation Maximization (MLEM) in the context of CC imaging.

Chapter 3 presents the tools needed to simulate the dual-panel CZT PET system. We present how GATE simulations work, what needs to be done with the output for validation of the experiment and input into the reconstruction algorithms. This is concluded by a short discussion on how the GATE data is implemented in a MLEM image reconstruction algorithm and the construction of the system matrix needed to reconstruct images.

We present our results in Chapter 4 where we reconstruct images of $^{44}$Sc, $^{72}$As, and $^{68}$Ga point sources and perform some analysis to asses their image quality. We then present results on a simulation of two point sources of $^{44}$Sc to demonstrate the ability to resolve two sources that are separate from each other.

We conclude our work by discussing future direction for this project. We present direction for either improving PET MLEM algorithms by joint-reconstruction methods including CC MLEM or improving PET image quality by CC informed PET image reconstruction for correcting positron range effects in conventional PET systems. We also discuss solutions to problems that are created by prompt-gamma emissions scattering within the energy window of positron annihilation photons in the form of quantum entanglement filtering of gammas.

## 1.1 Positron Emission Tomography

PET is an imaging modality under the large field of Computed Tomography (CT) in medical imaging. In PET, radionuclides are introduced into a patient in order to observe biological processes in what is referred to as *functional imaging*. X-Ray CT, depicted in Figure 1.1, in contrast to PET is an *anatomical imaging* technique where the radiation source is controlled externally from the patient through a medical device in order to image structural and anatomical information such as bone density. This works by measuring how the X-Ray intensity has decreased after passing through the patient and being absorbed by the detector.

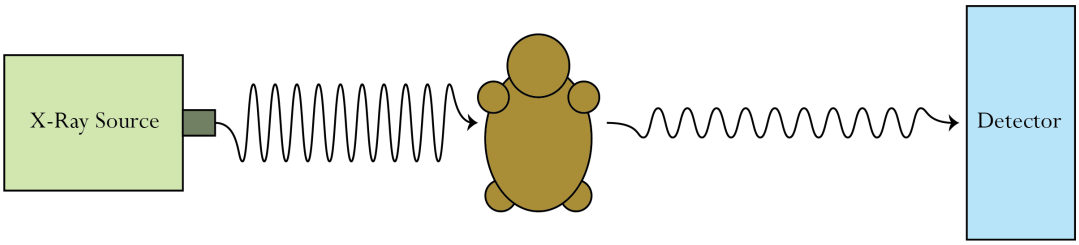


**Figure 1.1:** Demonstration of X-Ray CT. Radiation is transmitted through the target and the attenuated radiation is used to reconstruct the target image.

PET and ECT processes shown in Figure 1.2**A**, introduce radioisotopes to tracers that are injected into the patient's body where the tracers will accumulate at regions of interest such as cancerous tumors. The most common radionuclide in PET is Flourine-18 ($^{18}$F) which is introduced to a glucose molecule to create a radiotracer called 2-deoxy-2-[$^{18}$F]fluoro-D-glucose, or FDG. This is used primarily to detect and locate early development of cancerous cells and track the spread of tumor development by detecting the radioactive decay processes occuring after injecting the radiotracer within the patient. This is possible due to the metabolic processes of rapidly growing tumors uptake of glucose.

When a radioactive isotope is at a region of interest, during its decay the isotope will generate a positron which will travel a small distance before it interacts

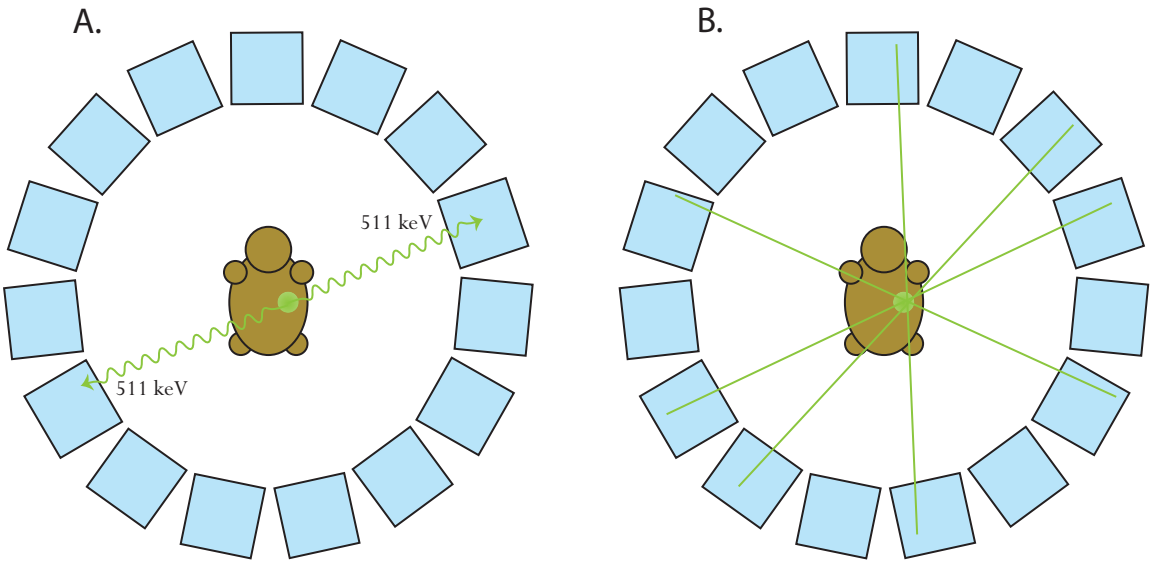


**Figure 1.2:** Demonstration of PET. **A**. Detectors record energy and position of incoming photons. **B**. Lines of Response (LOR) are drawn back over the imaging space from the measured data to estimate the location of the source.

with the surrounding tissue cells. This interaction with the tissue results in a process called positron annihilation where the positron combines with surrounding atoms (specifically their electrons) and gives rise to pairs of 511 keV photons which we call Positron Annihilation (PA) photons. These photons are emitted in opposite directions at nearly 180 degrees. This distance that the positron travels before annihilation is called the *positron range* and is a source of spatial inaccuracy PET that can vary among radionuclides.

Image formation is done through the coincident detection of PA photons which allows a line to be drawn between the detection locations that approximates the trajectory of the photon travel. As depicted in Figure 1.2**B**, from many detection events these lines can be drawn back over the imaging space. This line is what is called the Line of Response (LOR). Through the accumulation of many LORs the PET system can produce images using the LOR information to reconstruct and localize the radioactive distribution inside the patient.

PET performance can vary depending on the detector crystals used. PET is separated by two detector technologies: The first is *indirect conversion* detectors and the second is *direct conversion* detectors. Indirect detectors detect high energy photons through a conversion of the photon energy into optical photons and direct conversion detectors detect high energy photons through the movement of electrons through the crystal that are induced after being fully absorbed by the detector material. Direct conversion detector systems such as the CZT system presented in this work, can be succinctly characterized as having good energy resolution, high attenuation coefficients, but poor timing resolution. In contrast, indirect conversion detector systems have poor energy resolution compared to CZT but improved timing resolution. In short, timing resolution is a measure of how capable a system is in resolving arrival time differences between detected photons and energy resolution is a measure of how capable a system is in differentiating small differences in energy that is incident on the detectors [7].

An example of how indirect detector systems use their timing resolution to overcome its disadvantages is in *Time of Flight* PET (TOF-PET). In Figure 1.3 we can see that rather than drawing lines over the imaging space representing equal probability of activity as was represented in Figure 1.2, here we can localize and assign a probability density along the line. This is only possible for a system with small enough timing resolution. Although current CZT systems cannot do this as well as indirect detectors, our presented work in implementing a hybrid imaging modality to PET aims to contribute to improved performance of direct conversion detectors.

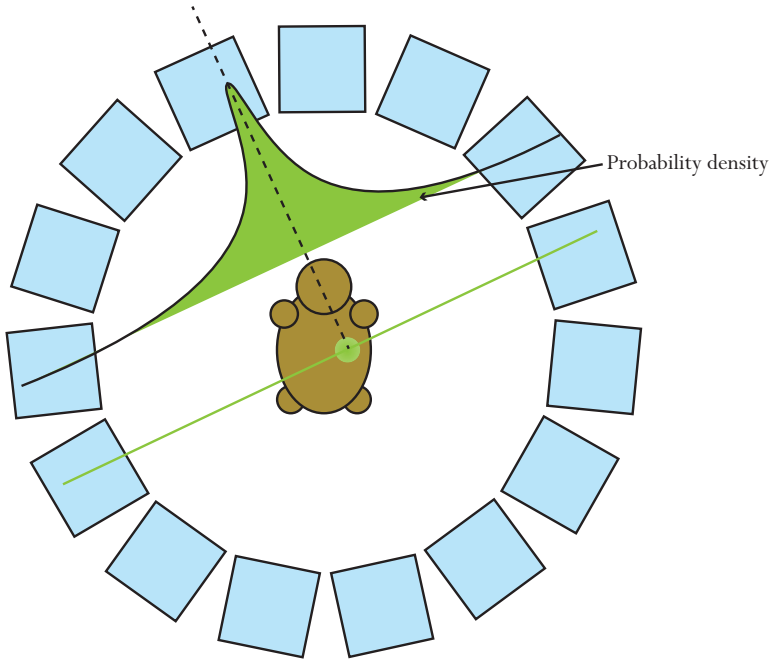


**Figure 1.3:** Time of Flight (TOF) PET. Distribution is localized along the line with timing information.

### 1.1.1 Photon-Matter Interactions in PET

The primary method in which PET operates is in the detection of photons via photoelectric absorption. Seen in Figure 1.4, when a photon is emitted from PA and travels through a detector medium, the nearby atoms fully absorb the incoming photon energy causing the ejection of an electron as a consequence. The electron in this case is referred to as a *photoelectron*, and is ejected with energy equivalent to the incoming photons energy minus the bonding energy for the electron. In nearly all cases the bonding energy is small compared to the annihilation photon's energy.

Another important photon-matter interaction that occurs as photons travel through a medium is Compton scattering. This can be seen in Figure 1.5. This interaction occurs when the photon passes and interacts with the outer shell orbital electrons of an atom. As opposed to photoelectric absorption, the photon

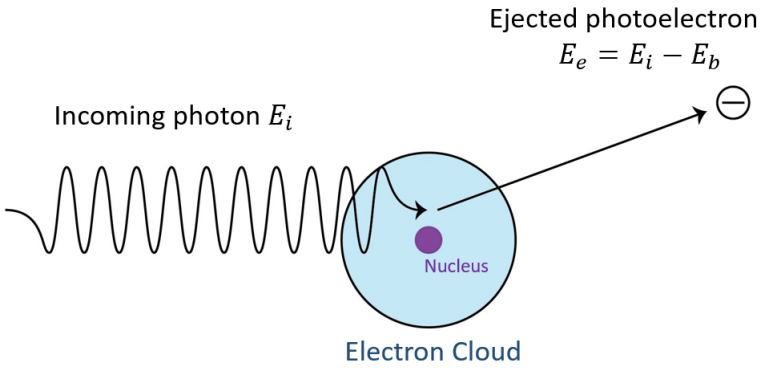


**Figure 1.4:** Photoelectric absorption

imparts only a fraction of its energy and causes the outer shell electron to recoil at an angle $\phi$ while the photon itself scatters at an angle $\theta$. This type of interaction is less desirable than photoelectric absorption when implementing PET. This type of interaction, when occurring within the patient, can become a large contributor to noise as it can create false LORs by scattering off the true LOR.

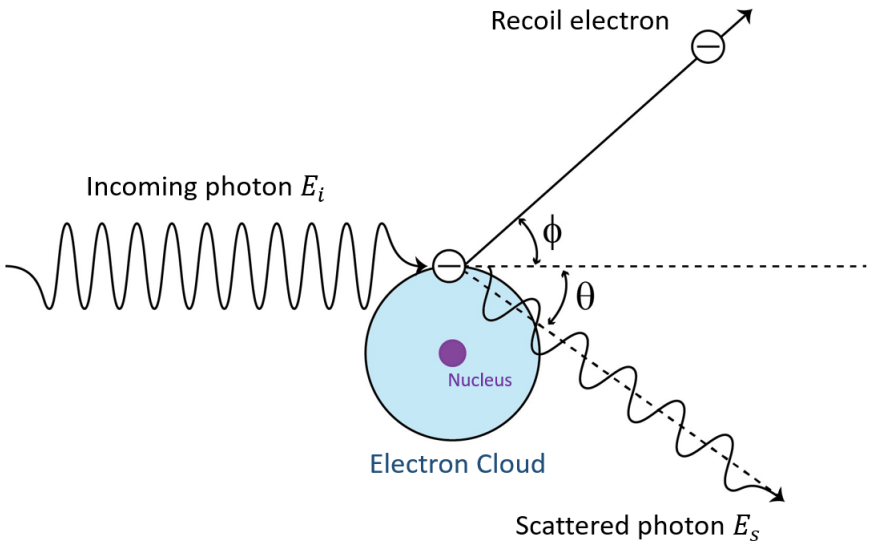


**Figure 1.5:** Compton Scattering

An important driver to Compton scattering is the incoming photon energy. We already know according to the Compton scattering equation that the angle

is dependent on the incoming energy, however, the interaction probability of the incoming photons can change depending on the energy which is described by the Klein-Nishina formula in the form of a differential cross section $\frac{d\sigma}{d\Omega}$. The unpolarized Klein-Nishina formula can be written in the following form

$$\frac{d\sigma}{d\Omega} = \frac{1}{2} r_e^2 \left(\frac{E_s}{E_i}\right)^2 \left[\frac{E_s}{E_i} + \frac{E_i}{E_s} - \sin^2(\theta)\right] \tag{1.1}$$

this equation describes a rate of incoming to outgoing flux of photons entering a differential area $d\sigma$ in which the photon will interact with nearby electrons and scatter into a solid angle area $d\Omega$. This is useful in that we can use it to determine through what polar scattering angles and what energies we expect to detect across our system. The ability for a detector to create accurate LORs and properly identify coincidences between photons will primarily be affected by Compton scattering interactions either within the subject or the detector [8].

### 1.1.2 Types of Coincidences

When two photons belonging to a pair of annihilation photons are detected in a PET system they are categorized as *coincidence* events. In the ideal world, all of the coincidences that a detector sees are *true coincidences*. That is, the coincidence photons detected in fact come from the same positron annihilation event. Below in Figure 1.6 we visualize three types of coincidences. We can detect *scatter coincidences* when either one or both of the annihilation photons undergo a Compton scattering event within the phantom or patient causing the trajectory to skew. Scatter coincidences lead to false LORs and can cause blurring in an image ruining the contrast if not properly filtered out. While annihlation photons arriving at the same time can be coincidences, one of these photons may be originating from a positron annihilation event in another part of the phantom leading

to what is called *random coincidences*. These types of coincidences can be hard to distinguish since both photons may have equivalent energies at approximately 511 keV, however, they will indeed cause blurring and in the ideal world would be filtered out.

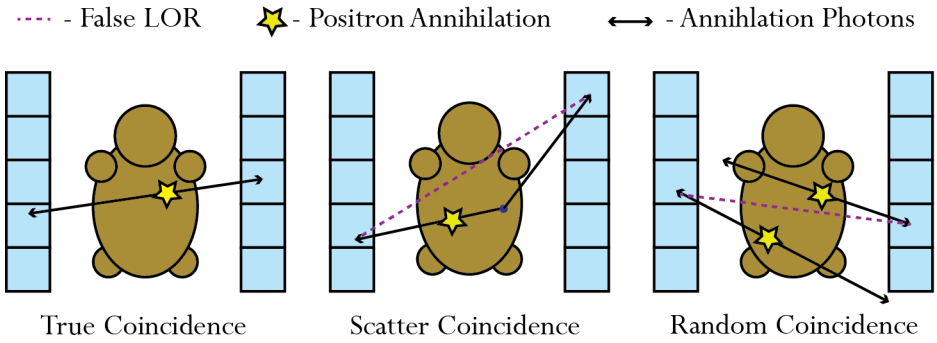


**Figure 1.6:** Coincidence types in PET

## 1.2 Single Photon Emission Computed Tomography

Single Photon Emission Computed Tomography (SPECT) is similar to PET in that the goal is to detect emitted photons from a radiotracer distribution inside a patient, however, the radiotracers used emit single photons of typically lower energies (100-300 keV) rather than annihilation photon pairs. SPECT devices are interfaced with collimators which allow for small acceptance angles for photons entering the SPECT detector therefore making it simple to map to a 1D line the activity distribution. We can see in Figure 1.7 how the prevention of incoming photons at oblique angles allows the approximation of a distribution of activity along a profile spanning the detector width. Typical applications of SPECT have a single detector panel that is then rotated 360° around the subject to gather line

profiles all around the subject. This can also be achieved with multiple detectors surrounding the subject, but in any case SPECT necessitates the full covering around the subject to have enough data to reconstruct an image.

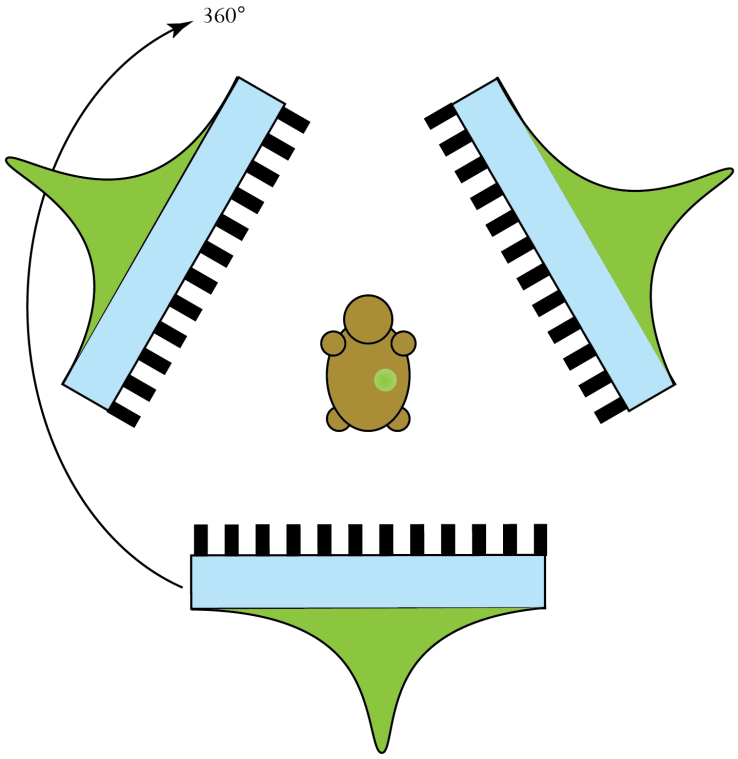


**Figure 1.7:** Demonstration of SPECT. The collection of 1D activity profiles around the subject at angles covering 360° allows the approximation of the location of radiotracer.

As opposed to PET, SPECT imaging operates in lower photon energies of around 100-200 keV requiring different materials and energy conversion techniques. Clinical SPECT systems can have energy resolutions as high as 10.0% to as low as 5.6% at energies of 140-160 keV which are what makes a large part of why SPECT systems are so useful for these use cases [9].

## 1.3 Compton Camera

Compton Camera (CC) is an alternative to SPECT in which the use of collimators and rotation of the imaging device is not necessary. The CC was first developed as a gamma camera in applications of astronomy known as a Compton Telescope [10]. The ability of Compton Cameras to detect photons from wider angles without collimators was first developed and coined as electronic collimation by Singh [11] [12] [13]. Collimatorless devices can lead to the potential implementation of multimodal imaging if the Compton kinematics necessary for Compton Cameras can be utilized within a standard PET system. We begin with a brief description of the physics of how a Compton Camera works and then review the current state of the art in Compton Camera systems.

Referencing Figure 1.8, typical implementations of the Compton Camera involve the use of two layers of detectors called the scattering layer and the absorbing layer. The idea is that photons will interact with the scattering layer of the detector made of a high Z material which aims to make Compton scattering the dominating photon interaction events in the detector. Photons interaction in the first layer allows one to define a $P_1$ event with associated energy, $E_1$, and position $(x_1, y_1, z_1)$. Subsequently, the absorbing layer's purpose is to absorb the scattered photon through photoelectric absorption. The absorbed photon at event $P_2$ will then have associated $E_2$ and $(x_2, y_2, z_2)$. The observation of these two subsequent events contain information needed to reconstruct Cones of Response (COR), an analogue to LOR in PET.

Solving the image reconstruction problem with a CC is done by utilizing the Compton kinematics that gammas undergo when interacting with the detector. Utilizing the position of the first Compton scattering event for a photon as well as the location of a subsequent photoabsorption of the scattered photon, a cone

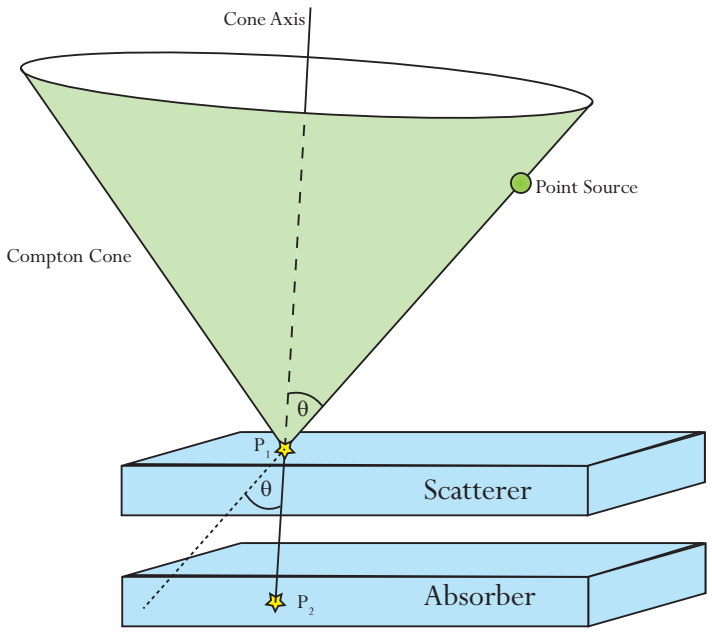


**Figure 1.8:** Demonstration of Compton Camera

beam projection can be evaluated and superimposed in order to reconstruct the origin of the gamma source. In this configuration of a gamma camera, as opposed to SPECT, the Compton Camera is a stationary device.

Detectors can record the energy and position of the first scattered photon that enters the detector volume and then record the energy and position of the subsequent photoelectric absorption of the photon in the volume. The Compton scattering equation

$$\cos\theta = 1 + m_e c^2 \left( \frac{1}{E_i} - \frac{1}{E_s} \right) \tag{1.2}$$

shows the relationship between the scattered energy $E_s$ and the initial incoming gamma energy $E_i$ with the scattering angle of the gamma, $\theta$. Therefore if a detector first sees an event with energy $E_1 = E_i - E_s$ and then a second event with energy $E_2 = E_s$ we can then create the Compton cone that is associated with this Compton scattering event and use this information to aid image reconstruction.

## 1.4 Hybrid Imaging

Here we will introduce state-of-the-art in approaches to improve features of PET and the problems that are being faced. We will first introduce the basics of radioactive decay physics and the different types of radiotracers of interest that motivate the pursuit of hybrid imaging systems. We will then highlight Scandium-44 ($^{44}$Sc), a radiotracer that is the central focus of this simulation work for demonstrating our CZT system's capability as a hybrid imaging tool. We will then discuss and highlight potential approaches to hybrid imaging that current literature shows.

### 1.4.1 Radioactive Decay Basics

#### Positron ($\beta^+$) Decay

In section 1.1 we introduced the most common radiotracer FDG and its radionuclide $^{18}$F. The basic process of positron emission occurs from a decay process of the radioisotope known as $\beta^+$ decay. The process can be succinctly written with the following equation

$$\mathrm{p}^+ \longrightarrow \mathrm{n} + \mathrm{e}^+ + v + \text{energy} \tag{1.3}$$

This shows the decay of a proton ($\mathrm{p}^+$) into a neutron (n) as well as the conversion of its mass to energy into a positron ($\mathrm{e}^+$) and neutrino ($v$). Neutrinos do not carry electric charge and leave the system without interacting with matter therefore this is of no interest to us. The positron is an anti-particle of an electron, essentially a positively charged electron, and is ejected from the point of decay with some kinetic energy depending on the isotope. When occurring within a patient, as depicted in Figure 1.9, the positron will travel imparting its kinetic

energy on surrounding atoms in the tissue of the patient until it either annihilates directly with an electron or comes to rest momentarily to form an atom with an electron called positronium. This positronium exists momentarily and has an associated *positronium lifetime* before it annihilates producing the familiar 511 keV PA photons [14].

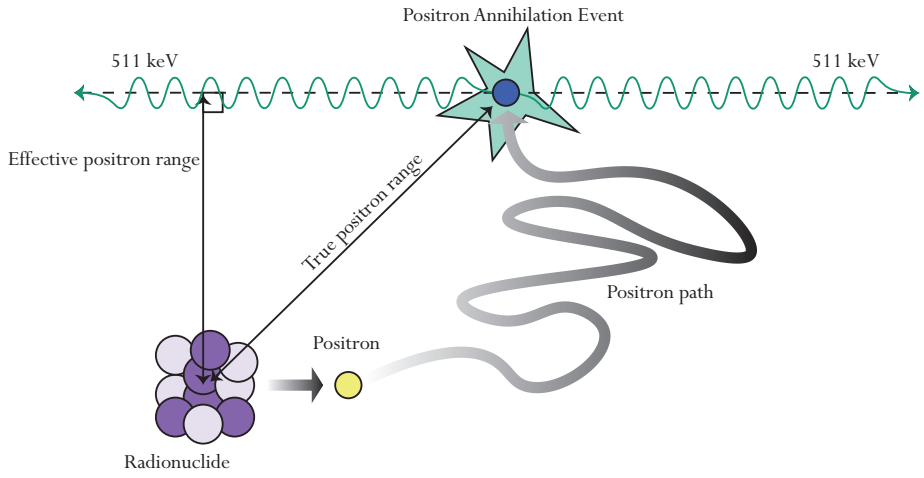


**Figure 1.9:** Depiction of positron-range in positron annihilation

### $\beta^-$ Decay

Another important mode of radioactive decay is that of $\beta^-$ decay. The decay is described as

$$\mathrm{n} \longrightarrow \mathrm{p}^+ + \mathrm{e}^- + v + \text{energy} \tag{1.4}$$

Therefore, in contrast to $\beta^+$ decay we see that a neutron decays into a proton and the conversion of energy goes into an electron ($\beta^-$ particle) and a neutrino. The energy from the $\beta^-$ particles are typically used in radiotherapy where the $\beta^-$ particle energy can kill cancerous cells from the absorption of the $\beta^-$ energy. Like $\beta^+$ decay, some isotopes that undergo $\beta^-$ decay can emit gammas in addition to $\beta^-$ particles allowing imaging of the radioisotope to be possible.

Referring to Figure 1.10, some isotopes undergo what is known as $\beta^+\gamma$ decay where the decay into a daughter isotope decays into an excited state which exists for some time $t_{1/2}$, before de-excitation to its ground state results in the emission of an additional photon known as a prompt gamma, $\gamma$. This is in addition to the positron which subsequently produces the PA photons.

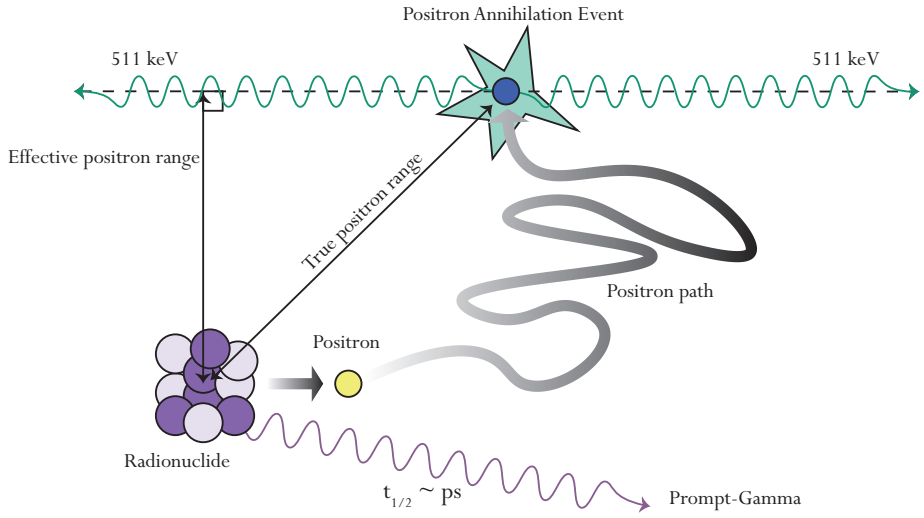


**Figure 1.10:** Depiction of positron annihilation with prompt-gamma emission.

This is specifically an area of interest for certain applications in which the prompt gamma can be a key identifier for a certain radiotracer which can be introduced into a patient in addition to another radiotracer which only expects to undergo $\beta^+$ decay. These conditions make *multi-isotope imaging* feasible if one were capable of differentiating one isotope from another using the prompt-gamma information [15] [16] [2]. Additionally, the prompt-gamma is key in providing timing information on when the time of decay occurs. Many prompt-gamma emitting isotopes, when decaying into their daughter isotope, have relatively small half-lives (on the order of a few ps) and provide much better information on the time of decay as opposed to positron annihilation photons. Research in this area are attempting to use the timing information provided by the prompt-gamma in

order to perform analysis such as correction for positron range or quantifying the lifetime of the positron in tissue [17].

Below in Table 1.1 we summarize the key attributes of some common prompt-gamma emitting isotopes along with F-18 for comparison [15] [18].

| Isotope | Half-Life | $\beta^+ E_{\text{ave}}$ (MeV) | $\beta^+$ Yield (%) | $\beta^+_{\text{ave}}$ Range (mm) | Prompt $\gamma$ (keV) | $\gamma$ Yield (%) |
|---|---|---|---|---|---|---|
| F-18 | 109.77 min | 0.250 | 97 | 0.62 | NA | NA |
| Sc-44 | 4.04 h | 0.630 | 94 | 2.46 | 1157 | 99.4 |
| Ga-68 | 67.7min | 0.836 | 89 | 3.56 | 1077 | 3.2 |
| As-72 | 26 h | 1.170 | 88 | 5.19 | 693 | 8.07 |
| | | | | | 834 | 81.0 |
| Zr-89 | 18.4 h | 0.396 | 23 | 1.27 | 909 | 99.0 |
| I-124 | 4.18 days | 0.687-0.974 | 23 | 3.37 | 603 | 62.9 |
| | | | | | 723 | 10.4 |
| | | | | | 1691 | 11.2 |

**Table 1.1:** Common prompt-gamma emitting radionuclides

### 1.4.2 $^{44}$Sc Application

With the prevalence of radiotherapy, the targeting of cancerous tumors with radioisotopes with the intent of killing the cancerous cells, the need to simultaneously perform dosimetry along with radiotherapy has become an area of interest for many in the nuclear imaging community. This combination of diagnostic imaging with therapy is called *theranostics*.

One common implementation of theranostics is in the treatment of metastatic prostate cancer. Metastatic prostate cancer produce what are called prostate-specific membrane antigen (PSMA). The attachment of radioactive materials to molecules with similar structures are called *radioligands* and these radioligands

have been found to accumulate in regions of prostate cancer. The most widely used radioligand for targeting PSMA in prostate cancer radiotherapy is Lutetium-177-PSMA ($^{177}$Lu-PSMA) [19]. $^{177}$Lu7 is primarily a $\beta^-$ emitting radioisotope which is used to kill prostate cancer cells. Although $^{177}$Lu emits some low energy $\gamma$ (113 keV at 6.4% and 208 keV at 11%) useful for SPECT, the yield is not great therefore image quality may not be the best. Most recent imaging diagnostic methods for aiding PSMA radiotherapy are done through **PSMA PET** using $^{68}$Ga and F-18 as radioligands. Research in finding appropriate radioisotopes for theranostics include ability to attach the isotopes to the molecules of interest and the half-life of the isotope. $^{44}$Sc is an isotope of interest for replacing $^{68}$Ga as a diagnostic since it has been seen to better resemble Lu-177-PSMA and its longer half-life makes its practicality for storage and transport better than $^{68}$Ga. Coincidentally, $^{44}$Sc has a smaller positron range by 1 mm on average compared to $^{68}$Ga making it better suited for PET.

## 1.5 PET-CC Imaging

In recent years many groups have invested into making systems that are capable of capturing prompt-gamma information and combining that data with conventional PET to correct for positron range effects. One approach proposed by Giovagnoli in 2020, based on a liquid Xe scintillation based detector with scattering and absorbing layers, coined *psuedo-TOF*, we can see in Figure 1.11 that the concept is use of the prompt-gamma COR intersection with LORs to assign a Gaussian distribution to the LOR similarly to what TOF PET does; however, in this case, the source is localized by the geometric information of when the prompt-gamma was emitted, which in many cases is on the order of picosecond delay from the time of positron annihilation [20] [21].

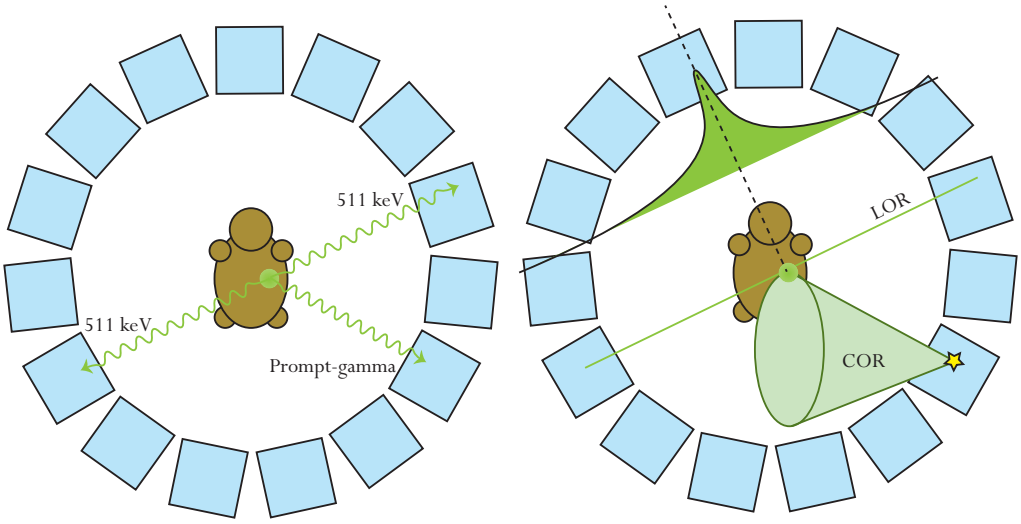


**Figure 1.11:** Depiction of $3-\gamma$ localization of source

The Jagiellonian PET (J-PET) group in Poland utilizes the same concept of the operation of PET with scattering-absorbing layers to induce Compton scattering to extract prompt-gamma information [17]. The J-PET system however has very good timing resolution capabilities and is more interested in using the timing information that they gather from prompt-gammas to gain further insight into positronium and orth-positronium formation in positron annihilation. As we mentioned before, in Section 1.4.1, when the positron is traveling through the tissue in a patient after a $\beta^+$ or $\beta^+\gamma$ decay event, the positron forms a particle called positronium momentarily [14]. This formation of positronium or even ortho-positronium is dependent on the atomic density of the tissue through which positrons travel and according to findings by Jasinska and Moskal there seems to be a correlation to the health of the surrounding tissue cells [22] [23]. J-PET is interested in making assessments on the positron lifetime using the prompt-gamma as a reference for when the positron emission occurred in order to provide more useful information for making cancer diagnoses using interesting techniques in triple coincidence detection of PA annihilation photons and prompt-gammas.

Many of these hybrid systems utilizing new image reconstruction modalities still require scattering and absorbing detector layers including the previously discussed systems. As visualized in Figure 1.12 we propose an existing high energy resolution CZT detector that has a sufficient detector thickness of 4 cm that is capable of detecting high energy prompt-gammas and thus being capable of collecting both PET and CC information for use in aiding reconstruction which can improve image quality in PET or be used for labeling and imaging multiple isotopes due to their prompt-gammas [24] [25].

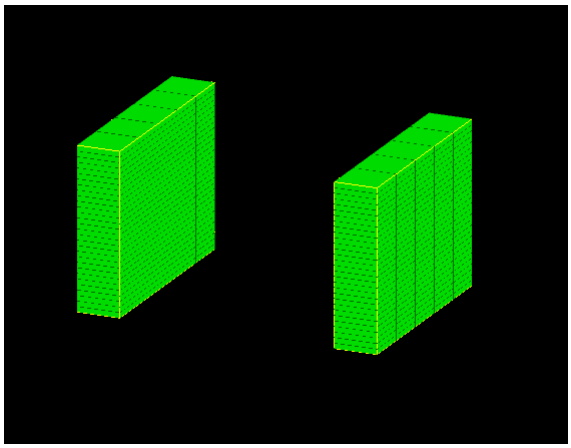

**Figure 1.12:** Simulation view of dedicated head and neck dual-panel CZT PET detector system

# Chapter 2

# Image Reconstruction

The work of this thesis includes the implementation of Compton Camera (CC) image reconstruction on an existing PET imaging system, this requires fleshing out the fundamental mathematics of nuclear medical image reconstruction for which this work is built upon. This chapter will cover the analytical models for the X-Ray and Radon transform which are the mathematical underpinning of how projection data is gathered in detector systems. This leads to the defining the Inverse Problem of the Radon transform which is central to that of PET, SPECT, and CC imaging. We will then motivate the examination of statistical models of the CC which is solved with iterative methods such as Maximum Likelihood Estimation - Expectation Maximization (MLEM).

## 2.1 The Inverse Problem

### 2.1.1 Beer-Lambert Law

As we introduced in Section 1.1, X-Ray CT is performed by transmitting a collimated beam of X-Rays through a subject to measure the attenuation of the beam at the detector side. We begin our discussion of the mathematical formulation of the X-Ray beam interaction with the scenario proposed by Natterer [26]. We set the stage with the transmission of a thin X-Ray beam as depicted in Figure 2.1 with initial intensity $I_0$ through the target material.

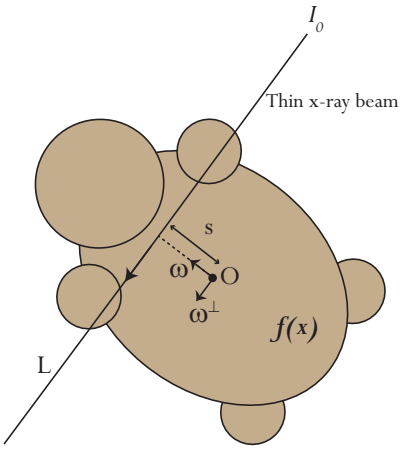


**Figure 2.1:** Thin X-Ray beam traveling through a subject.

The attenuation that the X-Ray undergoes as it travels through the material can be described as an unknown attenuation distribution function $f$ that describes the material through which the X-Ray is passing through. $f(x)$ is a real-valued function defined for $x$ in a 2-dimensional imaging space where $x \in \mathbb{R}^2$. As the X-Ray travels along the line, $L$, in the material through some positive $\delta x$, the Beer-Lambert Law describes the intensity loss of the X-Ray, $\delta I$, as

$$\frac{\delta I}{I} = -f(x)\delta x \tag{2.1}$$

This describes an Ordinary Differential Equation rewritten as

$$\frac{dI}{dx} = -f(x)I \tag{2.2}$$

This equation can be solved by standard separation of variables methods and we are left with the following integral representation of Beer-Lambert

$$\ln \frac{I_1}{I_0} = -\int_L f(x)dx \tag{2.3}$$

Where $I_1$ represents the intensity of the detected X-Ray after having passed through the target material and reached the detector. This equation says that the natural log of the ratio of the initial and final intensity of a single X-Ray beam is equivalent to the line integral along the path $L$ of the X-Ray that travels through the target material. In CT we are interested in approximating to the best of our abilities the spatial distribution function, $f(x)$, appearing in the integral of the RHS of (2.3). Thus in the case of X-Ray CT, the goal of image reconstruction is to invert the integral transform of $f(x)$.

The Beer-Lambert formulation for PET is similar to that of X-Ray CT and is proposed by Natterer in equation (2.4) below [26]

$$I = \exp\left\{ -\int_L \mu(y)dy \right\} \int_L f(x)dx \tag{2.4}$$

In the case of PET, we see an exponential attenuation of the line integral that appeared in the X-Ray formulation in equation (2.3). Here the function $\mu(y)$ represents the attenuation of $\gamma$ rays that are leaving the patient before they arrive at the detector. $f(x)$ in this case represents the radioactivity distribution in the imaging space. $I$ is the measured intensity of photons incident on a detector pair.

In PET reconstruction, the attenuation of photons within the subject is generally known and estimated and in many cases is neglected. For the sake of simplicity and to maintain the analogue to PET, we will assume $\mu$ is negligible and focus on the inversion of the integral in (2.3).

### 2.1.2 Radon Transform

Previously, we discussed Beer-Lambert integral representations describing the measured information of a single thin X-Ray beam in CT and a single annihilation photon pair in PET. A single data point alone would not be enough to reconstruct the entire spatial distribution of $f$ for X-ray CT and PET, therefore we must consider the entire set of line integral transforms of $f(x)$ in $\mathbb{R}^2$. This collection of line integral transforms is known as the **Radon transform**. Defined on the $n-1$ dimensional sphere and real line, for $\omega \in S^{n-1}$ and $s \in \mathbb{R}^1$, the form of the $n$-dimensional Radon transform is

$$\mathbf{R}f(\omega, s) = \int_{x \cdot \omega = s} f(x)dx \tag{2.5}$$

The $n$-dimensional Radon transform maps a function $f(x)$ defined for $x \in \mathbb{R}^n$ onto the set of integrals over the *hyperplanes* of $\mathbb{R}^n$. Hyperplanes are defined to be perpendicular to $\omega$ with a signed distance $s$ from the origin as shown by the vector product relation in the integral of 2.5. In the 2D imaging space for the Radon transform in $\mathbb{R}^2$, the hyperplanes of $\mathbb{R}^2$ are 1D lines along $\omega^{\perp}$. They represent a collection of thin beams of X-Rays a distance $s$ from the origin. In the case of PET, they represent a collection of lines created between detected photon pairs perpendicular to a distance $s$ from the origin.

In X-Ray CT, the distance $s$ is restricted to the capability for the detector to obtain perpendicular incident X-Ray beams and is thus restricted to the domain

$[-W, W] \in \mathbb{R}$ where $W$ is the half-width of the detector. In Figure 2.2 we can visualize the domain of $s$ restricted by the detector width. By letting $x = s\omega + l\omega^{\perp}$ we rewrite the integral in the second equality of equation (2.5) to show the parameterized imaging space of $x$ which allows us to simplify our understanding of $\mathbf{R}f(\omega, s)$.

$$\mathbf{R}f(\omega, s) = \int_{\omega^{\perp}} f(s\omega + l\omega^{\perp})dl \tag{2.6}$$

Given that the vector $\omega = \langle \cos\omega, \sin\omega \rangle$ for $\omega \in [0, 2\pi)$. We can make sense of evaluating the Radon transform as first taking a fixed value of $\omega$. Then taking integrals over $l \in (-\infty, \infty)$ spanned by $\omega^{\perp}$ for all values of $s$ which then gives us Radon values for a single angle. An example of this evaluation can be seen in Figure 2.2.

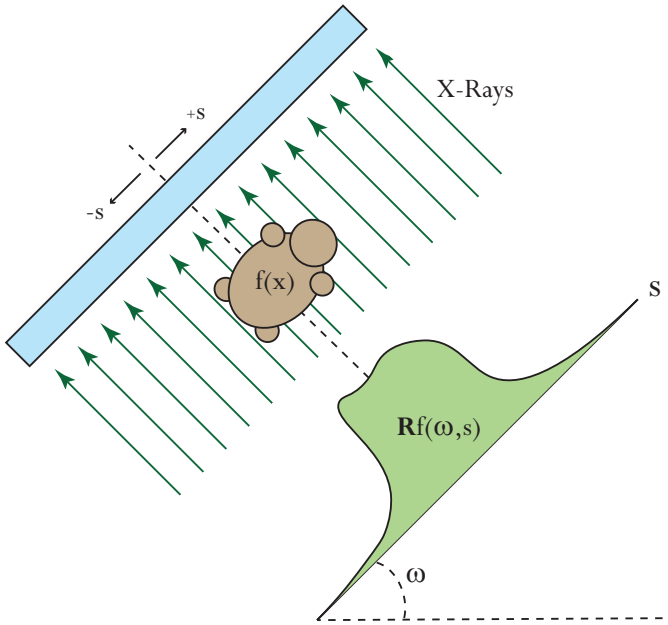


**Figure 2.2:** Radon Transform as projections in X-Ray.

We can understand the Radon Transform as taking projections over all angles

covering the subject. Much like how a tree casts a shadow by stopping photons and leaving a featureless representation of where it's located relative to the position of the sun, the subject leaves information of its position relative to the position of the detector between the X-Ray source.

One useful property to highlight about the Radon transform is that by observation of equation (2.5) we see that when $(\omega, s) = (-\omega, -s)$, $\mathbf{R}f$ is an even function on the product space $Z = S \times \mathbb{R}$ where $\mathbf{R}f$ lives. Meaning that $\mathbf{R}f(\omega, s) = \mathbf{R}f(-\omega, -s)$. This has the consequence that when implementing X-Ray CT, it is sufficient to gather projection data for $\omega[0, \pi)$ when implementing image reconstruction.

The Radon transform is what is termed the *forward problem* in the field of inverse problems as well as the *forward projection*. It is the mapping of the physical image characteristics onto a space of measurable data. In PET, the forward projection is the detection and collection of LORs. In CC, the forward projection is the detection and collection CORs. The goal of inverse problems is the mathematical inversion of the forward problem using the measured data to construct an estimate of the image in question.

## 2.2 Back-projection

One method that is fundamental to CT image reconstruction and can be seen implemented in various methods is back-projection. Back-projection as a mathematical operation is defined as the Radon operators adjoint. It has the property

$$\langle \mathbf{R}f, g \rangle = \langle f, \mathbf{R}^{\#} g \rangle \tag{2.7}$$

where

$$\mathbf{R}^{\#}g(x) = \int_S g(\omega, x \cdot \omega) d\omega \tag{2.8}$$

and $x \in \mathbb{R}^2$.

Since $\mathbf{R}^{\#}$ maps $S \times \mathbf{R} \mapsto \mathbf{R}^2$, one could naively view this as an inversion of $\mathbf{R}f$. If we wanted to define $g(\omega, s) = \mathbf{R}f$ and apply $\mathbf{R}^{\#}$ to $g$.

$$\mathbf{R}^{\#}\mathbf{R}f(\omega, s) = \int_S \int_{\mathbb{R}} f(s\omega + l\omega^{\perp}) dl d\omega \tag{2.9}$$

which demonstrates that by applying $\mathbf{R}^{\#}$ to $\mathbf{R}f(\omega, s)$, for fixed $\omega$, we are first integrating over the set of lines perpendicular to $\omega$. Next, for a fixed point $x$, we are integrating over $\omega$ the set of lines that intersect at the point $x$. Therefore, the function value at a point $x$ will be proportional to the sum of all of the projecting lines that intersect $x$. Applying the adjoint then leads to the following result

$$\mathfrak{B}f(x) = \mathbf{R}^{\#}\mathbf{R}f(\omega, s) = \int_S \int_{\mathbb{R}} f(s\omega + l\omega^{\perp}) dl d\omega = \frac{2}{|x|} * f(x) \tag{2.10}$$

This operation is called back-projection and is denoted as $\mathfrak{B}f(x)$.

This shows an approximation of the original source distribution $f(x)$ with a convolution blurring of some radial function $\frac{2}{|x|}$. We can demonstrate this by considering the ideal case where we are attempting to reconstruct a point source distribution modeled by the delta function $\delta(x)$ by letting $f(x) = \delta(x - x')$

$$\mathfrak{B}f(x) = \mathbf{R}^{\#}\mathbf{R}f(\omega, s) = \frac{2}{|x|} * \delta(x - x') \tag{2.11}$$

By the sifting property of convolution, with the point source located at $x' = (x_1, x_2)$, we get

$$\mathfrak{B}f(x) = \frac{2}{|x - x'|} \tag{2.12}$$

The estimation of $f(x)$ by the back-projection operator is a radial function $\frac{2}{|x-x'|}$ and is not the accurate image of the true distribution that we hope for when solving the inverse problem.

This is demonstrated below in Figure 2.3 where a single pixel is forward projected in a discretized version of the Radon Transform. The *sinogram* is the forward projection data in the $S \times \mathbb{Z}^{0+}$ domain for $\omega \in [0, \pi]$ and $s \in [0, 64)$. This data is then back-projected across the pixel imaging space and we recover a blurred version of the source image. Note the radial blurring of the back-projected image where the sharp features of the pre-image have been smoothed.

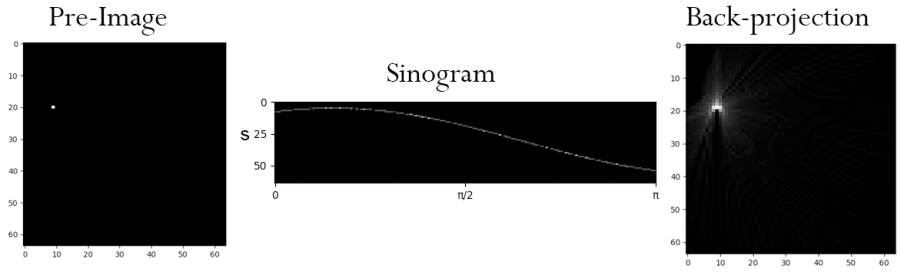


**Figure 2.3:** Forward projection, sinogram, and back-projection of a single point

Although not the best image quality is recovered from back-projection, it is the starting point for many common implementations of image reconstruction algorithms that are used in PET, SPECT, and CC imaging. We will not go into detail here about explicit inversions of the Radon Transform since the body of this work is implementing iterative inversion techniques.

## 2.3 Cone Transform

The formulation of the inverse problem for Compton Cameras is very similar to the X-Ray and PET case. Image reconstruction in CC Imaging requires the use of information that comes from the integration of surfaces of cones in $\mathbb{R}^3$ as

opposed to 2D line integrals in PET. Consider the event where a photon from a source incident on the detector scatters at a location $P_1$ in $\mathbb{R}^3$ and then interacts with the detector later at a location $P_2$.

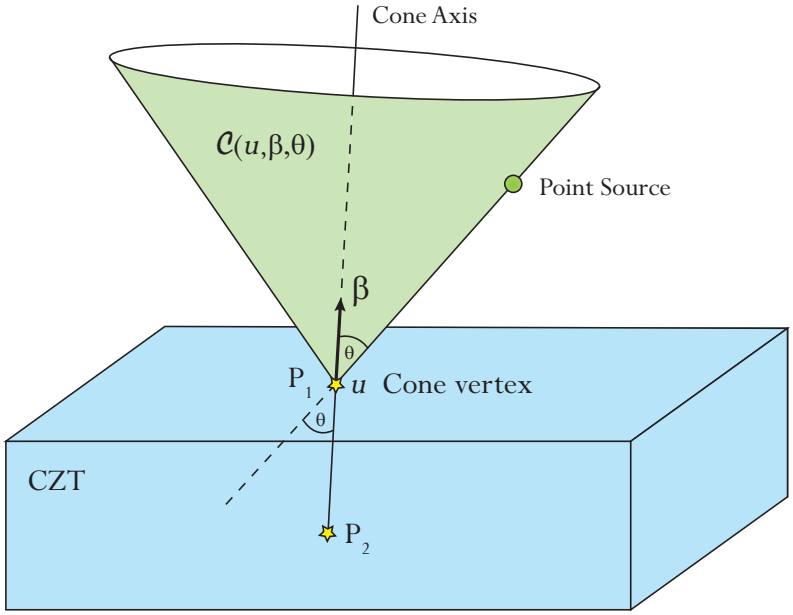


**Figure 2.4:** Construction of cone of response

Cones are defined by their location of vertex $u$, cone axis vector $\beta$, and half-open angle $\theta$ [27]. We therefore denote the sets of conic surfaces defined by these parameters as $\mathcal{C}(u, \beta, \theta)$. Let our source be defined by some real-valued function $f(x)$ for $x \in \mathbb{R}^3$ that describes the radioactivity distribution. We call the forward projection, or the transformed measured data, the cone transform defined as

$$Cf(u, \beta, \theta) := \int_{\mathcal{C}(u,\beta,\theta)} f(x) dS \tag{2.13}$$

with $u \in M$, $\beta \in S^2$, and $\theta \in [0, \pi)$. $M \subset \mathbb{R}^3$ is the detector set describing the space where vertices can be defined, and $S^2$ is the unit sphere. Now when taking into account the physics and statistical nature of the isotropic emission of gamma photons we see a modified version of equation (2.13) presented by Cree

and Bones [28]

$$Cf(u,\beta,\theta) = K(\theta, E_i) \int_{\mathcal{C}(u,\beta,\theta)} f(x) dS \tag{2.14}$$

where $K(\theta, E_i)$ is the Klein-Nishina coefficient as a function of the half-open angle $\theta$ and incident gamma energy $E_i$. Much work has been done involving the inversion of the cone transform in which a variety of derivations arrive at some form of extracting a Radon Transform of planes in $\mathbb{R}^3$ which already has well known explicit inversions [29]. In these works, it has been found that there is a much looser restriction on detector geometries in order to obtain sufficient data for unique reconstruction as opposed to PET. Tuy and others found that for unique reconstruction of cone data it is sufficient that any plane crossing the imaged object intersects the detectors of the system. This is a contrast to PET where we are restricted to lines that must intersect two opposing detectors [30]. The implications of this are that less data is needed for reconstruction and in the case of our two-panel system, two panels recover more than enough information for unique reconstruction.

## 2.4 Statistical Model

Analytic reconstruction models are not perfect. Models such as the Radon Transform do not accurately model and account for noise contributions in the reconstructed image and proper reconstruction assumes that there are infinitely many projections available. In the case of single panel or even double panel Compton Cameras the system is underdetermined as it is not possible to obtain all of the projection cones needed to cover the imaging space. One approach is to model the statistical nature of photon emission from radioactive isotope decays.

Below we will formulate a statistical model of prompt gamma emissions for the operation of a Compton Camera [31].

Take the image space where the true source distribution lies and divide the space into discrete boxes with associated probability of emission. We will have bins $i \in I$ where $I$ contains the detector bins for which the number of photons are counted in. We will then have $j \in J$ where $J$ contains the voxels that are defined in our imaging space. We can begin by defining $\mu_i = \sum_j t_{ij}\lambda_j$ where $\mu_i$ is the expected mean number of counts detected in bin $i$ given a Poisson variable $\lambda_j$ representing the activity in voxel $j$ and $t_{ij}$ represents the probability that data from bin $i$ originated from voxel $j$. The activity of photon emission from a radioactive isotope is a Poisson process. We introduce Poisson random variables $X_{ij}$ and $Y_i$ where $X_{ij}$ is the number of photons emitted by voxel $j$ that contribute to bin $i$ and $Y_i$ is the total number of photons recorded in bin $i$.

Given the mean value $\mu_i$ the conditional probability of seeing $Y_i$ take on the value $y_i$ is given by

$$p(y_i|\mu_i) = e^{-\mu_i}\frac{\mu_i^{y_i}}{y_i!} \tag{2.15}$$

In order to obtain the likelihood of the probabilities over all sets of bins $i$, since $Y_i$ for each $i$ are all independent random Poisson variables we can take the product over all bins and get the likelihood function

$$\mathcal{L}(y_i|\lambda) = \prod_{i\in I} p(y_i|\mu_i) = \prod_{i\in I} e^{-\mu_i}\frac{\mu_i^{y_i}}{y_i!} \tag{2.16}$$

The likelihood function is evaluating the joint probability distribution function of observing a given $y_i$ as a function of the parameters $\lambda$. In other words, what is the probability of observing a number of photons in bin $i$ given the source activ-

ity distribution $\lambda$ in our imaging space. The goal in a successful reconstruction algorithm is to found the $\lambda$ that maximizes this likelihood function according to the observed data that we measure in the detection process. Thus,

$$\hat{\lambda} = \arg\max_{\lambda} \mathcal{L}(y_i|\lambda) \tag{2.17}$$

Where $\hat{\lambda}$ is the value for $\lambda$ that maximizes our likelihood function. If we look at the likelihood function in the following form

$$\mathcal{L}(y_i|\lambda) = \prod_{i \in I} e^{-\sum_j t_{ij}\lambda_j} \frac{(\sum_j t_{ij}\lambda_j)^{y_i}}{y_i!} \tag{2.18}$$

we can see that maximizing $\mathcal{L}$ in the current form is not trivial. Fortunately, the arg max of the logarithm of a function is the same as the arg max of the function due to the monotonicity of log. This makes the optimization problem simpler since the log of products is the sum of the log of the individual terms.

$$\log(\mathcal{L}(y_i|\lambda)) = \log\left(\prod_{i \in I} e^{-\sum_j t_{ij}\lambda_j} \frac{(\sum_j t_{ij}\lambda_j)^{y_i}}{y_i!}\right) \tag{2.19}$$

$$= \sum_{i \in I} \log\left(e^{-\sum_j t_{ij}\lambda_j} \frac{(\sum_j t_{ij}\lambda_j)^{y_i}}{y_i!}\right) \tag{2.20}$$

$$= -\sum_{i \in I}\sum_j t_{ij}\lambda_j + \sum_{i \in I} y_i \log\left(\sum_j t_{ij}\lambda_j\right) - \sum_{i \in I} \log(y_i!) \tag{2.21}$$

So replacing $y_i = \sum_j x_{ij}$ gives the log-likelihood function defined as

$$\mathbf{L}(\mathcal{L}(\lambda)) = \log(\mathcal{L}(x_{ij}|\lambda)) = -\sum_{i \in I}\sum_j t_{ij}\lambda_j + \sum_{i \in I}\sum_j x_{ij} \log\left(t_{ij}\lambda_j\right) - \sum_{i \in I}\sum_j \log(x_{ij}!) \tag{2.22}$$

and we can update the problem statement of finding $\hat{\lambda}$ to be

$$\hat{\lambda} = \arg\max_{\lambda} \mathbf{L}(\mathcal{L}(\lambda) \tag{2.23}$$

The non-linearity of the log-likelihood function in application to emission tomography does not have an explicit solution, therefore iterative optimization methods are used to solve for $\hat{\lambda}$. The most common of which being the **Expectation Maximization** (EM) algorithm [32] [31], [33]. The algorithm has two steps:

1. Finding the expectation of the log-likelihood.
2. Maximizing the resulting expectation by setting the first derivative of the expectation equal to zero.

Beginning with the expectation step (1) on equation (2.22) is taking the conditional expectation of the log-likelihood given parameters $y_i, \lambda$

$$E(\mathbf{L}(\mathcal{L}(\lambda))|y_i, \lambda) = -\sum_{i \in I} \sum_{j} t_{ij}\lambda_j + \sum_{i \in I} \sum_{j} E(x_{ij}|y_i, \lambda) \log(t_{ij}\lambda_j) - E(\log(x_{ij}!)|y_i, \lambda) \tag{2.24}$$

The expectation term of the last term is constant and will be denoted as $C$ while the expectation term in the second term is

$$E(x_{ij}|y_i, \lambda) = y_i \frac{t_{ij}\lambda_j}{\sum_{k \in J} t_{ik}\lambda_k} \tag{2.25}$$

The maximization step (2) is done by differentiating equation (2.24) with respect to $\lambda_j$ and equating to zero to find the $\hat{\lambda_j}^{(\ell)}$ that maximizes where $\ell$ is the iteration

step.

$$\frac{\partial}{\partial \lambda_j} E(\mathbf{L}(\mathcal{L}(\lambda_j))|y_i, \hat{\lambda_j}^{(\ell)}) = -\sum_{i \in I} t_{ij} + \sum_{i \in I} E(x_{ij}|y_i, \hat{\lambda_j}^{(\ell)}) \frac{1}{\hat{\lambda_j}^{(\ell+1)}} = 0 \tag{2.26}$$

$$\hat{\lambda_j}^{(\ell+1)} = \frac{\sum_{i \in I} E(x_{ij}|y_i, \hat{\lambda}^{(\ell)})}{\sum_{i \in I} t_{ij}} \tag{2.27}$$

This leads to the iterative solution of the EM algorithm

$$\hat{\lambda_j}^{\ell+1} = \frac{\hat{\lambda_j}^{(\ell)}}{\sum_{i \in I} t_{ij}} \sum_{i \in I} \frac{t_{ij} y_i}{\sum_{k \in J} t_{ik} \hat{\lambda_k}^{(\ell)}} \tag{2.28}$$

In implementation, we first compute $\sum_{k \in J} t_{ik} \hat{\lambda}_k^{(\ell)}$ with an initial estimate of $\hat{\lambda}_k^{(\ell)}$ and system matrix $t_{ij}$ summing the product components over every voxel in $J$. This is known as the forward projector. Recalling that our original definition for $\sum_j t_{ij} \lambda_j = \mu_i$ as the expected mean number of photons we hope to see in detector bin $i$, then using an initial estimate $\hat{\lambda}^{(\ell)}$ we define the quantity in the denominator of equation (2.28) as $y_i^{(\ell)}$. Meaning we are predicting our observed $y_i$ given an initial or $\ell$th guess for $\hat{\lambda}_j^{(\ell)}$. Next, we take a ratio of the current measured projection data $t_{ij} y_i$ with the previously computed forward projection for each bin $i$ to get a notion of how far off our $\ell$th estimation of the activity distribution is from our measured set. Summing over all of these ratios for each bin $i$ and multiplying the result with $\hat{\lambda}_j^{(\ell)}$ is the backprojection operation which after normalization by $\sum_{i \in I} t_{ij}$ gives us our $\ell + 1$ estimate for the activity and the algorithm is iterated until either a set number of iterations are performed or until some measure of error between the measured and estimated activity is satisfied.

In list-mode (LM) MLEM, each measurement taken by the detector is considered a unique bin, therefore the measurement vector $y_i = 1$ for detected events and $y_i = 0$ for $i \notin I$ [33]. Therefore the LM-MLEM formulation provides a

computational advantage and is now defined as

$$\hat{\lambda_j}^{\ell+1} = \frac{\hat{\lambda_j}^{(\ell)}}{\sum_{i \in I} t_{ij}} \sum_{i \in I} \frac{t_{ij}}{\sum_{k \in J} t_{ik} \hat{\lambda_k}^{(\ell)}} \tag{2.29}$$

This formulation is the same for both PET and CC image reconstruction and implemented similarly. Description of how this is implemented will be discussed in Chapter 3.

# Chapter 3

# Simulation of a dual-panel detector

Here we detail the experimental setup of a simulation study of an existing two-panel CZT PET detector. This study involves a monte carlo simulation of a variety of point source models of prompt gamma emitting radionuclides in order to quantify the capability for an increased sensitivity in the PET detector if operating as a Compton Camera (CC). We will discuss how a GATE simulation is set up and run within the context of this experiment. After GATE simulations are performed, the data is processed into a List Mode (LM) format. We will then discuss the details of the implementation of a open source GPU accelerated Compute Unified Device Architecture (CUDA) LM-MLEM image reconstruction algorithm.

## 3.1 GATE

GATE (Geant4 Application for Tomographic Emission) is an software application for simulating high energy physics interactions with detectors [34]. It is built off of Geant4 which is a software developed at CERN for simulating particle interactions with matter for applications in high energy physics, nuclear physics, or particle accelerators [35]. This simulation platform allows for the generation and validation of detector materials and geometries in order to get a sense of the "perfect world" capabilities of a detector before putting the resources into the construction of the physical system. In Figure 3.1, we present a flowchart that demonstrates the steps that the user takes when defining a GATE simulation.

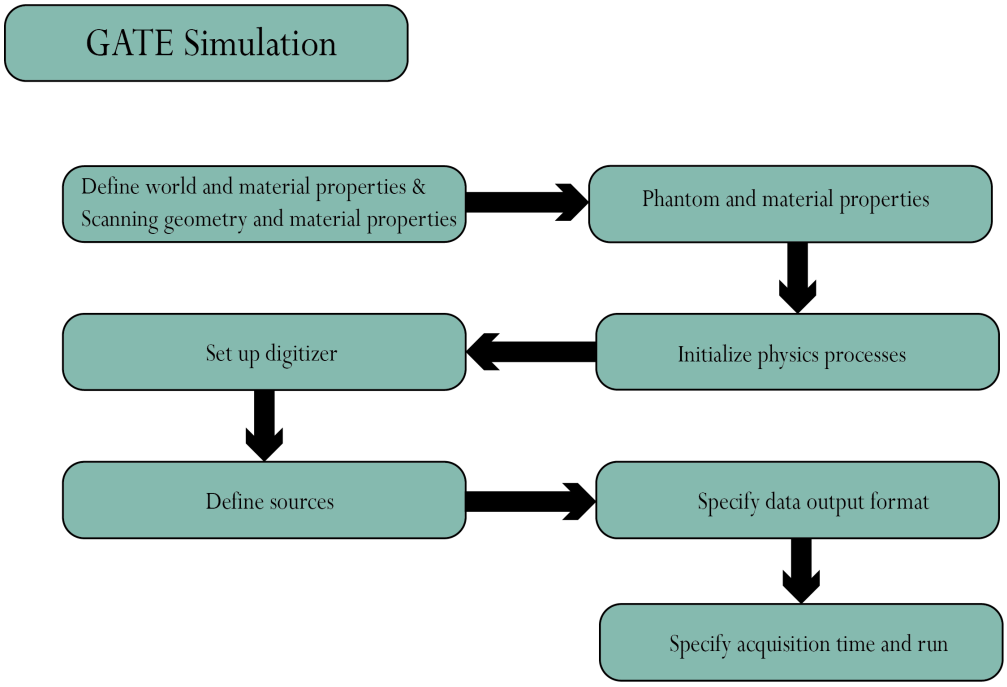


**Figure 3.1:** Steps for initialization and running a GATE simulation.

First, GATE simulations require the construction of *volumes* which contain information about dimensions and material so that GATE can track particles and their material interactions. In GATE we first begin with the construction

of a *world* volume which encompasses the space in which GATE will simulate and record information about the physics and particle interactions. The detector geometry is built within the *world* volume and a hierarchy of volumes are created with the *world* as the highest level and its daughter volumes are the sections of the detector which we wish to construct. In our experiment we constructed a model of the dual-panel CZT detector.

Once the geometry and all of the associated volumes are constructed, the physics processes to be simulated must be specified according to the application. This specification allows GATE to know which physical particle-matter interaction and behavior to simulate and record. In our experimental setup we use the `em_standard_opt3` physics list which contains the necessary electromagnetic interactions of photons of energies up to 10 MeV with the detector material in addition to activating radioactive decay physics which is required to simulate the radionuclide decay physics.

After the desired physics interactions are specified, GATE offers a digitizer module which allows the simulation of readout electronics in sorting the interactions detected. In our experiment we opted not to use this module as we wish to have apriori information about all of the processes occurring in our detector system. We also opt out of the digitizer to implement our own post-simulation file processing to sort our compton cone information.

After the digitizer, GATE requires that the user define the radionuclide sources to be simulated. GATE has the freedom to create phantoms with user defined geometries and composed of various materials where one can place radioisotopes within. There is great flexibility in defining sources with GATE and one can even mimic radioactive decaying isotopes through simple mono-energetic gamma emission definitions that GATE provides. When simulating sources, one must

define the source activity which is measured in Becquerels (Bq). Bq is an SI unit describing *decays per second*. Thus, an isotope with 1 Bq of activity will undergo radioactive decay 1 time every second according to its decay scheme. In this study we define point source spheres of 0.1 mm radius with 2 MBq of activity using the ion source definition of the radioisotope 44-Scandium ($^{44}$Sc) as well as the simulation of two other radioisotopes, 68-Gallium ($^{68}$Ga) and 72-Arsenic ($^{72}$As).

After the simulation scene has been set, we can specify where and in what format our data is output in. GATE can record information associated with every particle interaction it simulates and can output this information in a binary or ascii file called a *Hits* file. The final step before running a simulation is specifying the acquisition time that GATE will simulate. The acquisition time specified in this experiment was 1 second.

## 3.2 Dual-Panel CZT System

The detector system we simulate is based off of direct conversion semiconductor CZT crystals which offer full width half maximum (FWHM) energy resolutions as low as 4.33% $\pm$ 0.30% in the existing experimental system [36]. Visualization of the construction of our Dual-Panel detector in GATE is provided in Figure 3.2. The CZT dimensions are $4 \times 4 \times 0.5\text{cm}^3$. The panels are constructed with 5 columns of 30 CZT crystals stacked on top of each other to create a detector panel area of $20 \times 15\text{cm}^2$. The panels are spaced at a distance of 20cm from detector face to detector face.

The field of view (FOV) of the detector system is centered about the point $(0, 0, 0)$ in coordinate space. The current experiment sees two $^{44}$Sc point sources with 0.1 mm radius centered at (-5.5,0,0) and (5.5,0,0) within the FOV. The

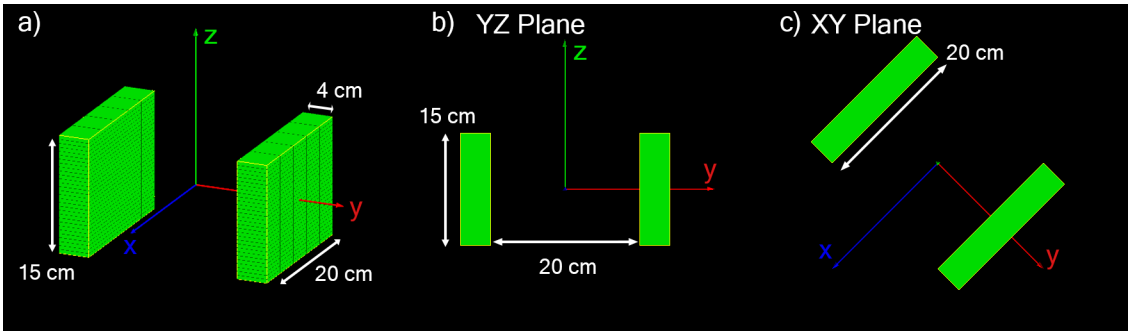


**Figure 3.2:** Detector system geometry visualized in GATE

advantage of this CZT system for this experiment is the edge-on orientation of the CZT crystals. Most direct conversion PET systems have pixelated faces and the thickness that photons travel through the detecting crystal is a few mm. Since CZT has a high cross-section of Compton scattering interactions, the 4 cm of detector thickness allows this system to scatter prompt-gammas and detect their scattered direction within the same crystal or across multiple crystals at a higher rate than conventional PET systems. The implication of this is that there is no need for constructing a scatter-absorber detector geometry to implement CC imaging, which would be a costly addition to a CZT system of this size.

## 3.3 Compton MLEM

After acquiring a hits file we process the data and create a List-Mode file containing the COR information (Energy and Position information of scattering and absorption events) for input into an MLEM code. Referring to (2.29) in Chapter 2, the reconstruction method used is the following MLEM algorithm

$$\hat{\lambda_j}^{\ell+1} = \frac{\hat{\lambda_j}^{(\ell)}}{\sum_{i\in I} t_{ij}} \sum_{i\in I} \frac{t_{ij}}{\sum_{k\in J} t_{ik}\hat{\lambda_k}^{(\ell)}} \tag{3.1}$$

This reconstruction is implemented in Compute Unified Device Architecture (CUDA) for speed up by parallel computation given that the system matrix and number of computations can be very large.

### 3.3.1 System Matrix

Typically the system matrix is constructed via the forward projection of the acquired data from the detector system. The details of how the forward projection is carried out can vary. In the method in this work, the construction of the system matrix $T$ is determined by determining the voxel-cone intersections of the cones measured by the detector system and integrating them. Through the recording of the position and energy deposited from the first compton scattering event along with the position and energy deposited from the subsequent photoelectric absorption event, the measured compton cone can be defined as $\mathcal{C}_j(u, \beta, \theta)$ where $j$ is the $j$th measured compton cone out of a total of $J$ measured cones. Every cone is defined by its vertex $u$, unit vector describing the cone axis $\hat{\beta}$, and the half-open angle $\theta$.

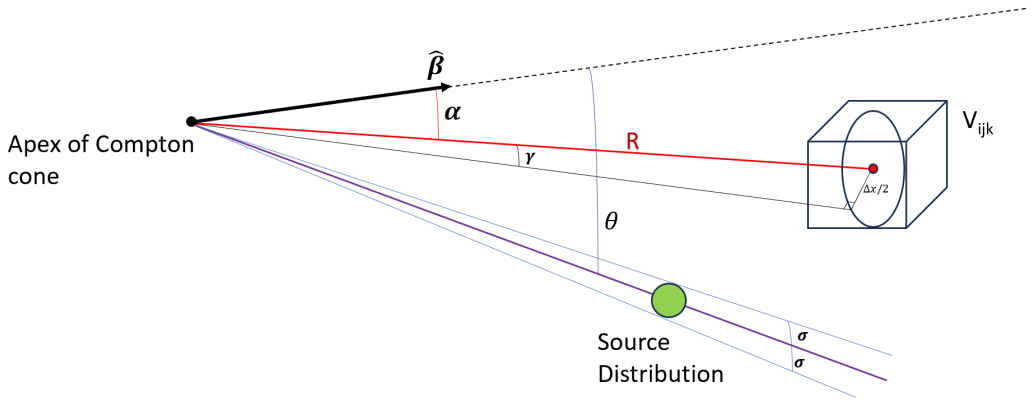


**Figure 3.3:** Diagram showing the relative location of voxels to the cone of response

The most difficult part of MLEM is the construction of the system matrix $t_{ij}$.

Lojacono outlines a number of methods in which integration of the CORs can be carried out [37]. One of those methods proposed were implemented in following formulation of $t_{ij}$

$$t_{ij} = Cf(u, \beta, \theta) = K(\theta, E_i) \int_{\mathcal{C}(u,\beta,\theta) \cap V_j} f(x) dv \tag{3.2}$$

where the integral in (3.2) is taken over a volume element $dv$ resulting from the set of all $I$ number of cone surfaces $\mathcal{C}(u, \beta, \theta) = \{\mathcal{C}_i(u, \beta, \theta);\ i = 1, ..., I\}$ that intersect with a given voxel $V_j$. In Figure 3.3 we graphically set the scene for determining the intersection of cones. When any segment of the voxel is near the measured $\theta$ we call this an intersecting cone-voxel pair. We define an arbitrarily small angle $\sigma$ around $\theta$ and when the voxel falls within $3\sigma$ of $\theta$ we integrate over the intersecting bounds. This occurs when $|\theta - (\alpha \pm \gamma)| < 3\sigma$. In fact, $\theta, \sigma$, define parameters for a Gaussian function estimating the probability density of the activity distribution within the volume enclosed by the cone of response. This Gaussian function is seen implemented in various ways in other literature, for example as a mix double Gaussian, however in this case a single Gaussian is used [38] [39]. This leads us to rewrite (3.2) as along with a visual representation of the bounds of integration of the cone thickness below in Figure 3.4.

$$t_{ij} = K(\theta, E_i) \int_A \int_{\varphi_i}^{\varphi_f} f(\vartheta) \sin(\vartheta) dA \tag{3.3}$$

where

$$f(\vartheta) = e^{-\frac{(\vartheta-\theta)^2}{2\sigma^2}}$$

and $f$ is identically zero for $\mathcal{C}_i \cap V_j = \varnothing$ The bounds for integration and values of $\varphi_i$ and $\varphi_4$ will depend on whether a portion of $3\sigma$ surrounding $\theta$ does not intersect the current voxel $V_j$. Otherwise, $\alpha \pm \gamma$ will be used as either the upper or lower bounds of integration.

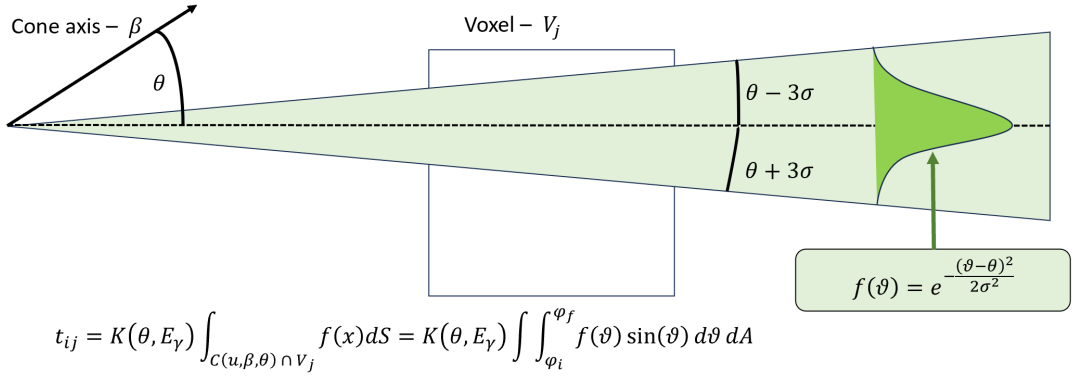


**Figure 3.4:** Graphical representation of the integration along the thickness of a cone-voxel intersection

Although there are various methods for the numerical computation of the area element of the voxel-cone intersection, what is implemented in this MLEM algorithm is a simplified voxel-center method outlined by Lojacono [37]. The remaining parts of integration are carried out as the width and height defined by the voxels for intersecting cones. An important parameter in the accuracy of this reconstruction is the standard deviation $\sigma$ parameter chosen in this method. This standard deviation value and Gaussian distribution function may be seen as representing the angular uncertainty (as a consequence of uncertainty in the energy measured) in the measured and computed half-open angle $\theta$ from the prompt-gamma information [40]. Therefore the image quality is going to suffer if angular resolution is poor. In this implementation all results obtained, otherwise noted, correspond to an energy uncertainty in $\pm 10$ keV.

# Chapter 4

# Results

## 4.1 GATE Simulation

The first results we present are GATE simulations of $^{44}$Sc, $^{68}$Ga, and $^{72}$As for the dual-panel system. All three isotopes are simulated in GATE separately as 0.1 mm radius spheres with activity of 2 MBq for an acquisition time of 1 second. Each simulation placed the point sources 10 cm from each panel at the center of the field of view and origin of the coordinate space (0,0,0). The results for the energy deposited on the CZT system for the three isotopes can be seen below in Figure 4.1. This is a validation of GATE's ability to simulate the decay schemes and associated gamma emissions of these various isotopes. All three isotopes show peaks at 511 keV where the detector is fully absorbing the annihilation photons via photoelectric absorption. We observe the different prompt-gamma emissions among the three isotopes as well. For example, $^{72}$As has at 834 keV with an intensity of 81% of $\beta^+$ decays and at 693 keV with an intensity of 8%. We also note the lower counts seen in $^{68}$Ga comparatively with the other two isotopes. This should follow from the 89% intensity of $\beta^+$ decays along with the small intensity of 3% of $\beta^+$ decays leading to 1.077 MeV prompt gammas.

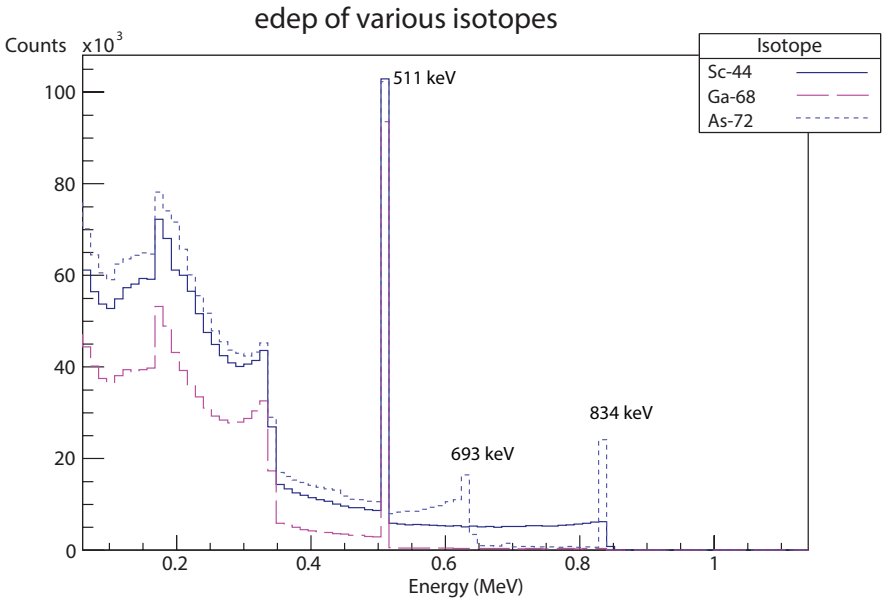


**Figure 4.1:** Energy deposition comparison of $^{72}$As, $^{68}$Ga, and $^{44}$Sc

With GATE we can also plot the separately the different interactions that are happening with CZT such as the photoelectric absorption and Compton scattering. In Figure 4.2 we see the photoelectric absorption peak at 511 keV with a distribution of photoelectric absorption centered at about 190 keV. The spectrum we see above 511 keV belongs to the spectrum of scattering energies of the high energy prompt-gamma due to the physics described by the Klein-Nishina formula. These extra Compton scattering interactions represent an increased sensitivity in the system for use with CC imaging.

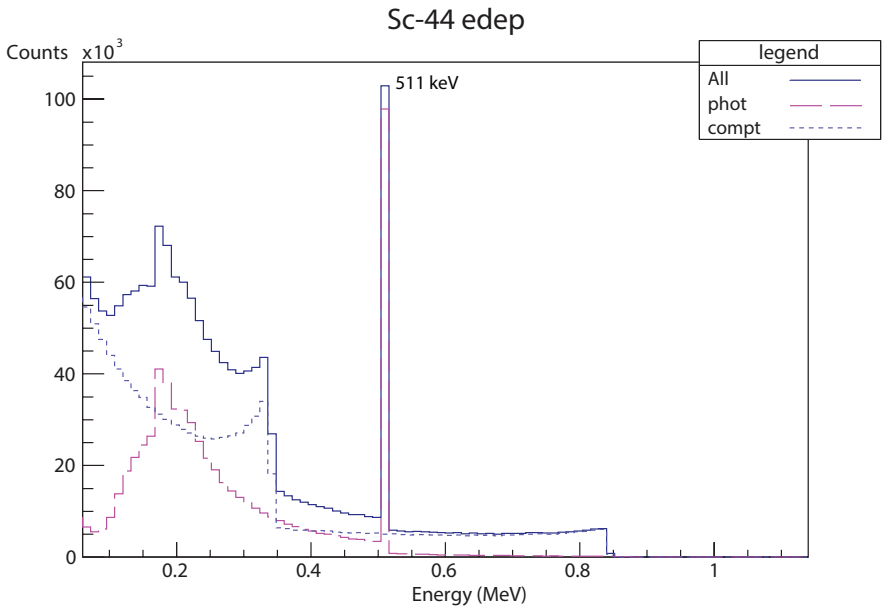


**Figure 4.2:** Comparison of energy deposition of photoelectric absorption and Compton scattering

## 4.2 Point Source Compton MLEM Reconstruction

Beginning with the single point source GATE simulations of the 0.1 mm spheres for 2 MBq of $^{44}$Sc, $^{72}$As, and $^{68}$Ga we were able to detect at least 10,000 Compton cones for $^{44}$Sc and $^{72}$As while obtaining approximately 300 Compton cones for $^{68}$Ga. The imaging space in the following reconstruction is a $20 \times 20 \times 20$ mm$^3$ space made up of $640,000$ voxels. Each direction is made of 40 voxels and the voxel size of the imaging space is $1 \times 1 \times 1$ mm$^3$.

Below in Figures 4.3, 4.4, 4.5 with $\sigma$ uncertainty in the cone-thickness corresponding to 1 keV we plot CC image reconstruction along with PET image reconstruction of the same point source runs for all three isotopes. Figures 4.3, and 4.4 for $^{44}$Sc and $^{72}$As used 10,000 Compton cones for reconstruction and were reconstructed after 20 iterations. Figure 4.5 for $^{68}$Ga was reconstructed with only

300 cones due to the low prompt-gamma yield of 3% per positron decay. We can see some activity around the central distribution in the PET images that correspond to positron range effects with those features being more pronounced for something like $^{72}$As which has a larger mean positron range of approximately 5 mm. In the case of Figure 4.3 with $^{72}$As, we see the CC image have a stronger localization of the point source with some barely visible artifacts that may be due to improper implementation of the CC image algorithm which was used. We can see in Figure 4.5 for $^{68}$Ga that with the low number of cones obtained although the main estimation is nearly correct and can be seen to be more distinguished than the PET, the overall image quality in this implementation of MLEM shows many artifacts compared to the other results.

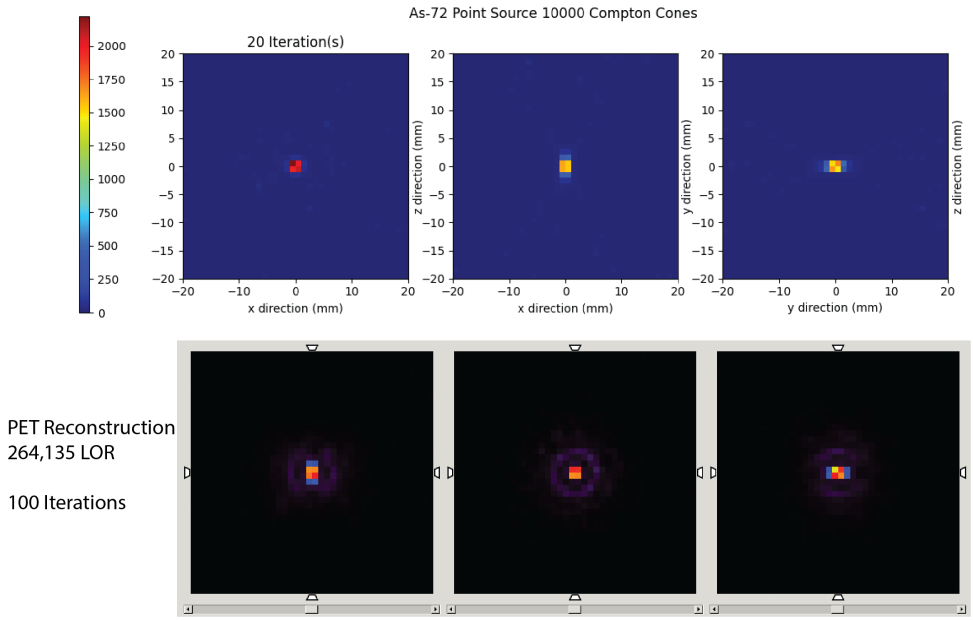


**Figure 4.3:** PET and CC image reconstruction comparison for $^{72}$As of a 0.1 mm radius point source placed at (0,0,0)

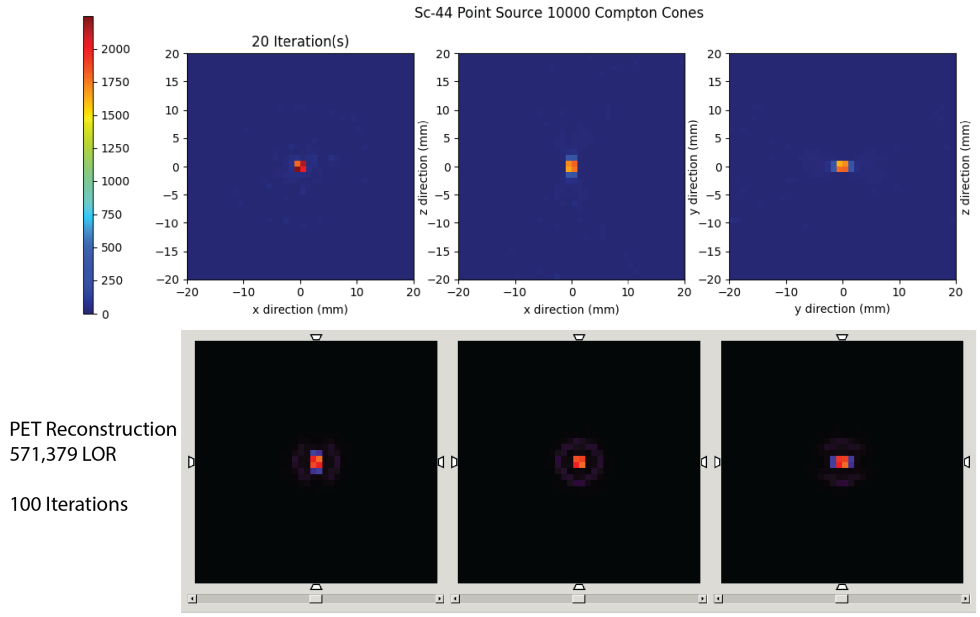


**Figure 4.4:** PET and CC image reconstruction comparison for $^{44}$Sc of a 0.1 mm radius point source placed at (0,0,0)

In figure 4.6 we reconstruct point sources of $^{44}$Sc with 1000 cones, $^{72}$As with 1000 cones, and $^{68}$Ga with 300 cones after 20 iterations of MLEM, however this time we add some uncertainty to the cone thickness in $\sigma$ with 10 keV. Although the GATE simulation gives ground truth information on location and energy deposited, we implement this uncertainty to understand the extent of image degradation in CC imaging. Each isotopes values were normalized across the three planes and we see that the largest contrast in image quality is seen in the xz plane. Visually, $^{44}$Sc has better image quality in all three planes as well as larger values for the estimates as the colorbar axes show.

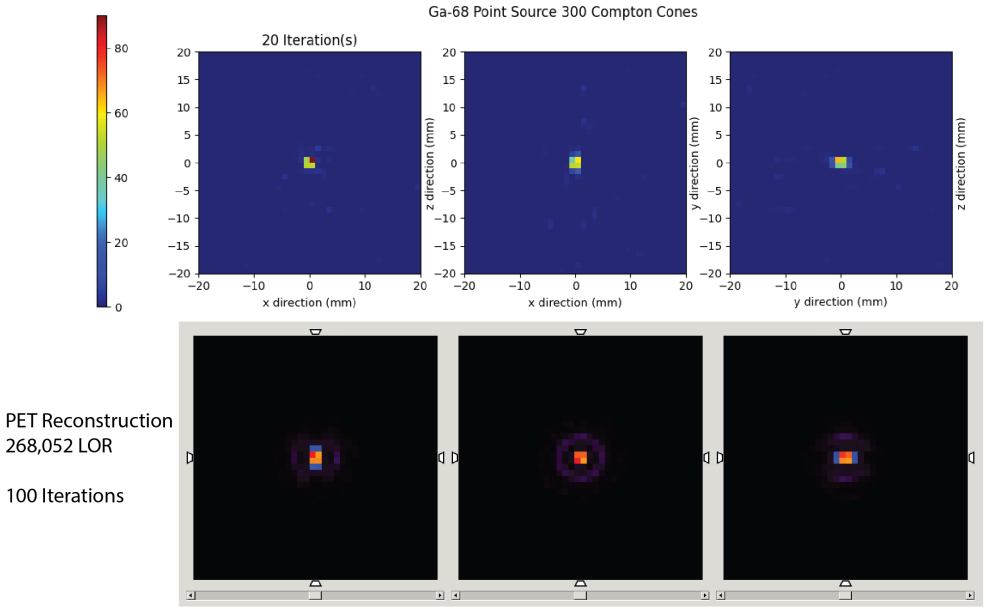


**Figure 4.5:** PET and CC image reconstruction comparison for $^{68}$Ga of a 0.1 mm radius point source placed at (0,0,0)

We plot the normalized activity values along the $x$-profile below in Figure 4.7 and fit Gaussian curves to the data and compute the full width at half maximum (FWHM) of the x profiles for each of the isotopes. We report a FWHM of 2.453 mm for $^{44}$Sc, 4.419 mm for $^{72}$As, and 3.358 mm for $^{68}$Ga.

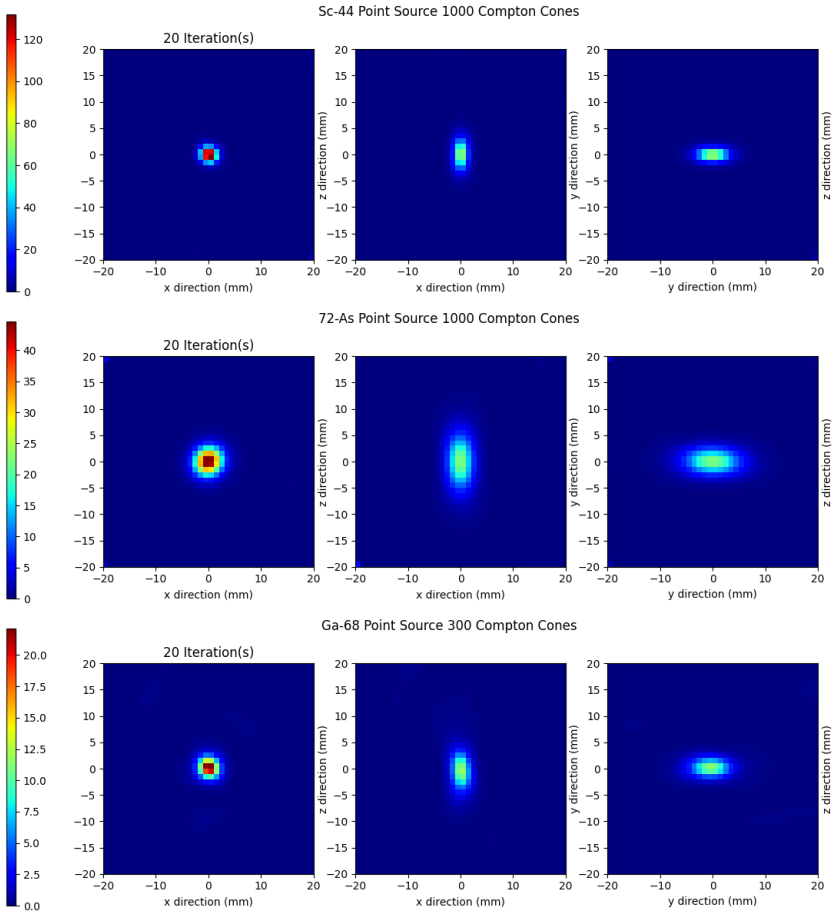


**Figure 4.6:** Reconstruction of 0.1 mm radius point sources

We continue the analysis further in Figure 4.8 of the quality of image reconstruction by plotting the computed FWHM at each iteration of MLEM for the point sources in the x direction for each isotope. We conclude that after 10 iterations the increased improvement in FWHM begins to deteriorate and that 20 iterations is sufficient.

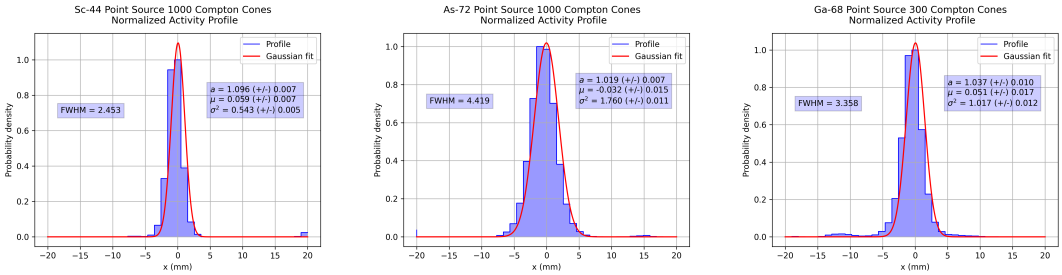


**Figure 4.7:** Normalized activity profile in $x$ with FWHM of 2.453 mm for $^{44}$Sc, 4.419 mm for $^{72}$As, and 3.358 mm for $^{68}$Ga after 20 iterations with Gaussian fits, $f(x) = ae^{-\frac{(x-\mu)^2}{2\sigma^2}}$.

The improvement in FWHM of $^{44}$Sc over $^{68}$Ga and $^{72}$As is 0.905 mm and 1.97 mm respectively. Recalling the mean positron range for each isotope; 2.46 mm for $^{44}$Sc, 3.56 mm for $^{68}$Ga, and 5.19 mm for $^{72}$As, in the perfect world, our estimates reflect the physics that prompt-gamma emission information is unaffected by positron range effects. We then present results on the effects of the number of Compton cones used for MLEM in Figure 4.9. The results show no meaningfully significant improvement in FWHM over all of the iterations.

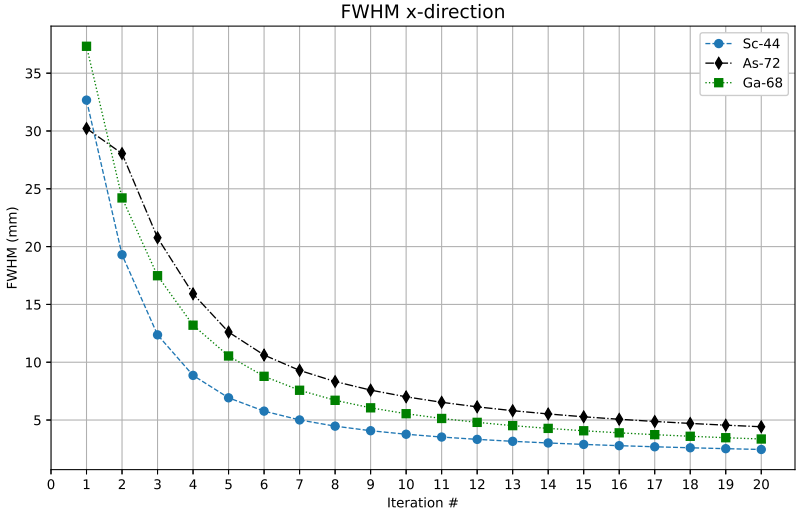


**Figure 4.8:** FWHM as a function of iteration number in the $x$-direction for $^{44}$Sc, $^{72}$As, and $^{68}$Ga

To conclude these results we show a comparison of the FWHM of each profile for $^{44}$Sc in Figure 4.10. FWHM values for the $x$ and $z$ direction are comparable and the FWHM values in the $y$-direction is significantly poor in the first few iterations but converges to a value closer to the $x$ and $z$ directions.

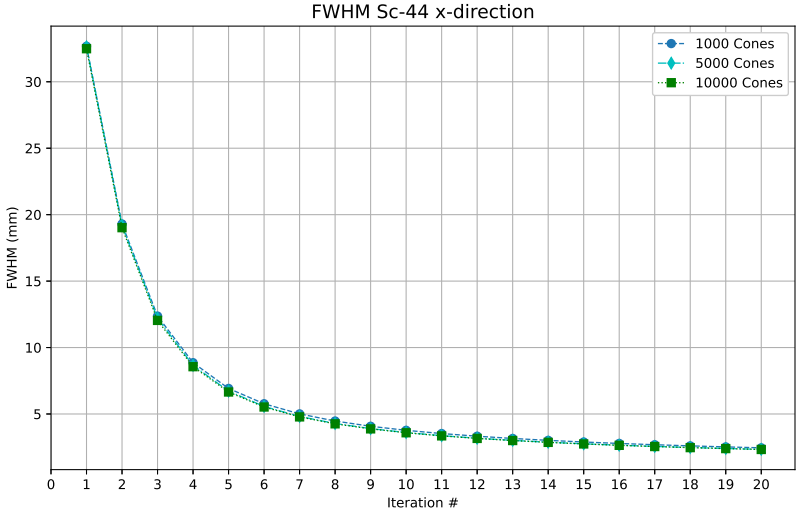


**Figure 4.9:** FWHM as a function of iteration number in the $x$-direction for $^{44}$Sc for various numbers of Compton cones used for MLEM.

## 4.3 Two Point Sources Reconstruction $^{44}$Sc

The next experiment involved the image reconstruction using MLEM CC reconstruction on two $^{44}$Sc 0.1 mm radius point sources with activity of 1 MBq each placed 10 mm center-to-center from each other at (-5.5,0,0) mm and (5.5,0,0) mm. We begin with a reconstruction using $\sigma$ corresponding to an energy uncertainty of 1 keV and providing a comparison to the PET image reconstruction of the same simulation in Figure 4.11.

In Figure 4.12 we plot the image reconstruction of the two point sources at each iteration over 20 iterations of MLEM in the $xz$ plane with 10,000 Compton cones. All images are normalized by the min and max of the last iteration. The two point sources emerge after iteration 8 but start to become contrasted after iteration 10. In Figure 4.13 we then plot the normalized profiles with Gaussian fits in the $x$ direction to get a better visual on how the point sources are becoming distinguished. We observe that at iteration 9 the peaks of the two point sources are

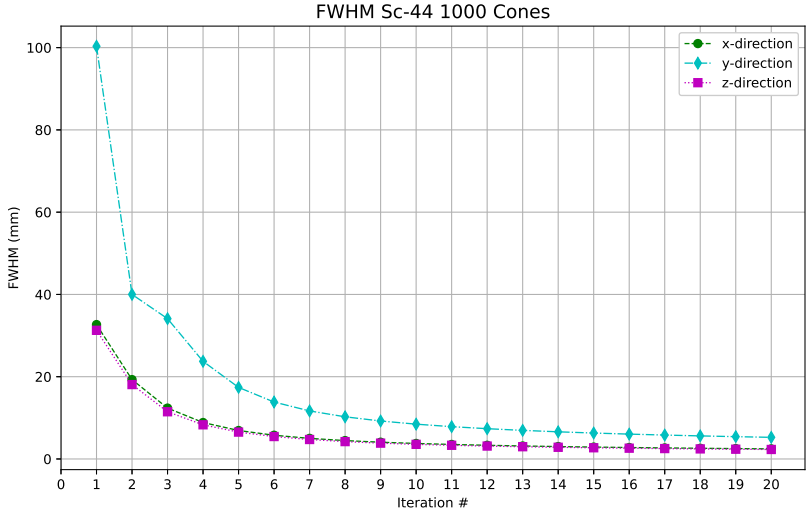


**Figure 4.10:** FWHM as a fucntion of iteration number in $x$, $y$, and $z$ directions for 1000 Cone MLEM reconstruction of $^{44}$Sc.

at least twice as large in amplitude than the activity distribution valley between them.

We then plot our image reconstruction after 20 iterations of the three different planes in Figure 4.14. We observe the best image quality in the $xz$ plane with the activity profile in the $xy$ plane having the worst quality. We plot a normalized acivity profile at iteration 20 of these three profiles in Figure 4.15 and from the Gaussian fits compute FWHM of 2.746 mm, 6.279 mm, and 2.807 mm in the $x, y$, and $z$ directions respectively. The FWHM in the $x$ profile of the double Gaussian peak is taken as the average of the calculated FWHM of the individual peaks. We point out that in many of our reconstructions that there seems to be a smear or elongation of the activity distribution in Figures 4.6 and 4.14. This smearing appears in the $y$ direction which is in the direction orthogonal to the detector faces. This is an effect that is also seen in PET due to limited angle artifacts, being that the detector being comprised of two flat panels doesn't provide total angular coverage and is missing projection data [41]. This is elongation as it is called in

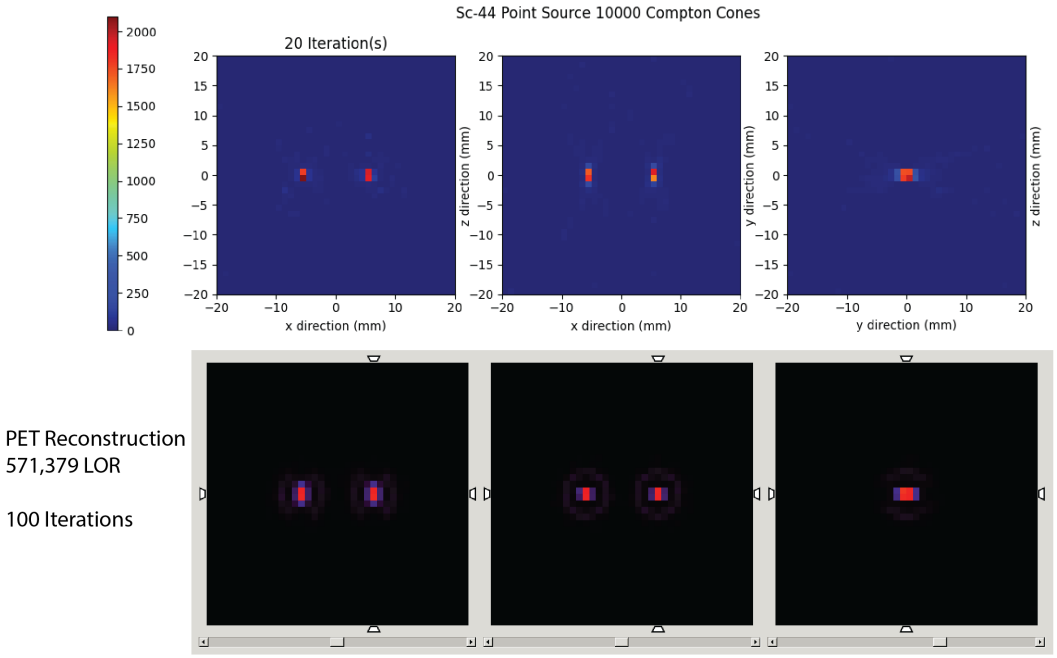


**Figure 4.11:** PET and CC image reconstruction comparison for $^{72}$As of two 0.1 mm radius point sources placed 10 mm apart at (-5.5,0,0) mm and (5.5,0,0) mm

literature is an artifact that is seen in many Compton cameras [42] [43] [20].

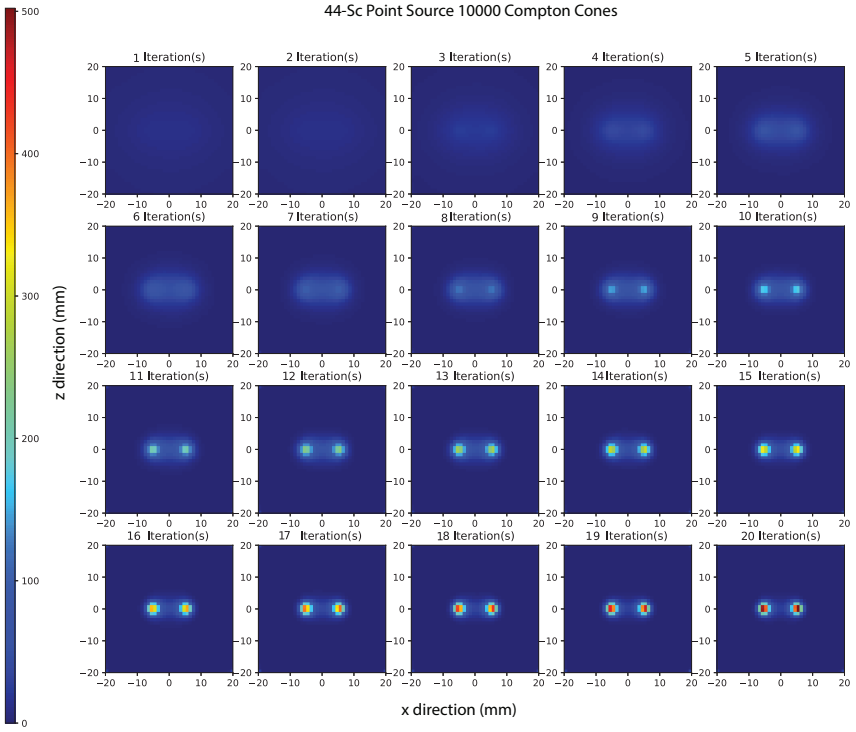


**Figure 4.12:** $^{44}$Sc MLEM Reconsruction of the $xz$ plane over 20 iterations of MLEM with 10,000 Compton cones

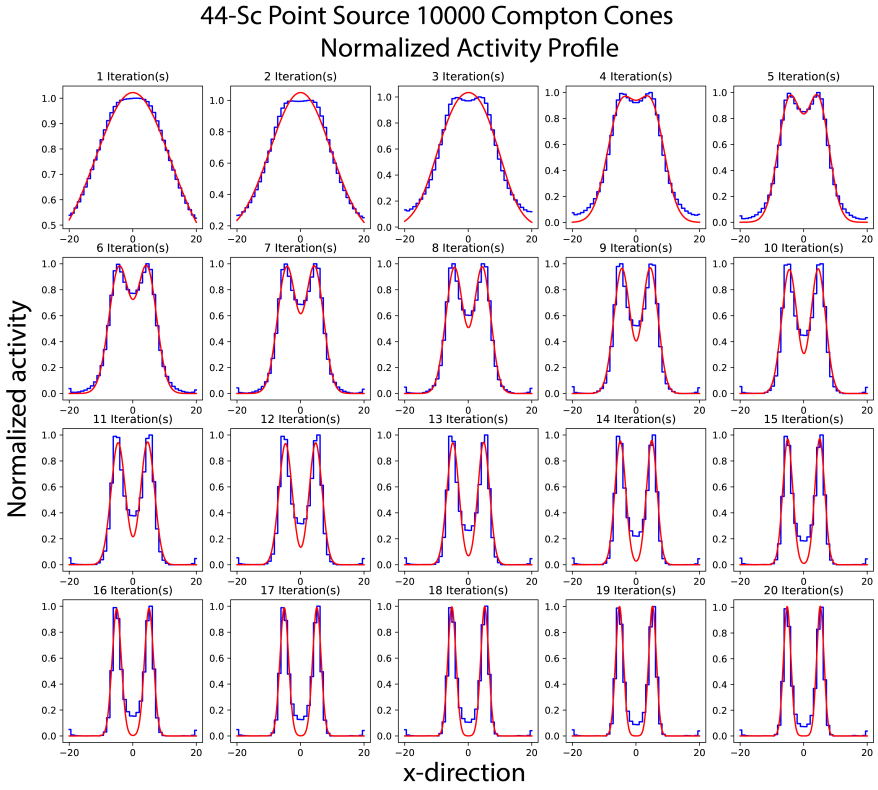


**Figure 4.13:** Normalized profile with Gaussian fit in the $x$ direction over 20 iterations of two 2 MBq $^{44}$Sc point sources placed at (-5.5,0,0) and (5.5,0,0)

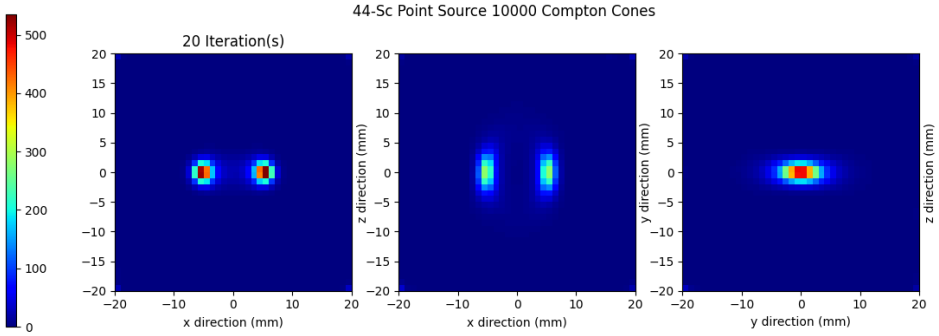


**Figure 4.14:** Image reconstruction of all three planes of two point sources of $^{44}$Sc after 20 iterations using 10,000 Compton cones

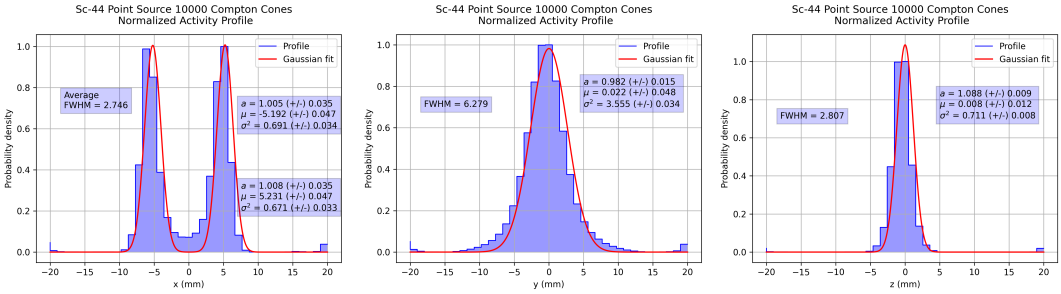


**Figure 4.15:** Normalized activity profile in $x, y$, and $z$ with Gaussian fits. The FWHM are 2.746 mm, 6.279 mm, and 2.807 mm in the $x, y$, and $z$ directions respectively

# Chapter 5

# Discussion

What we've demonstrated is that simply due to the capability for CZT to detect high energy interactions from prompt-gamma emitting radioisotopes, the dual-panel PET detector systems inherent advantages allow it to be a capable dual-imaging modality device as a PET and CC imaging system. We implemented for the first time on this PET system CC imaging reconstruction of various prompt-gamma emitting isotopes with profile FWHM of up to 4.419 mm. We've demonstrated that this system is capable of taking advantage of the Compton kinematics of prompt-gammas for potential use as a hybrid imaging device. Two potential directions for future work are available for us.

The first is taking inspiration from the current state of the art where a modified MLEM for the current PET system can be implemented. Using the Compton scattering information from prompt-gammas current MLEM could be modified to construct system matrices $t_{ij}$ with LOR and COR intersections over the imaging space.

The second direction is an alternative to real-time PET-CC image reconstruction, but rather using CC image reconstruction to inform PET reconstruction. Since the spatial accurate of CC imaging in negating positron range effects, rather

than event-by-event basis reconstruction of PET-CC, one could use the estimation and statistical variance from the CC image reconstruction to make corrections to the range effects of PET. Another advantage of separate PET-CC imaging modalities is the ability to perform multi-isotope imaging and additional work in improving the modeling of detector geometry for improving the limited angle artifacts.

Some pitfalls for our future work may come in the way of polluted data for PET reconstruction. With additional gammas from prompt-gamma emitting isotopes where high energy gammas can be emitted along with nearly every positron decay, the 511 keV window could be polluted by high energy gammas scattering with energy falling into the annihilation photon energy window. Potential solutions to this could involve taking advantage of the high scattering cross section of the CZT system to filter false LORs of random and scatter coincidences from prompt-gammas using quantum entanglement properties of annihilation photon pairs [44]. With whatever sensitivity is gained and lost by imaging prompt-gamma emitting isotopes, these potential quantum entanglement properties of annihilation photons could create in increase in sensitivity for a hybrid imaging system that isn't seen in any current prompt-gamma PET systems. Our results and experiment are a preliminary for many more exciting investigations in taking emission tomography systems to another level.

# Bibliography


[1] "PET exam number United States 2020," *Statista*. [Online]. Available: https://www.statista.com/statistics/962242/pet-examinations-in-united-states-total-number/

[2] Y.-J. Lee *et al.*, "89Zr-panitumumab Combined With 18F-FDG PET Improves Detection and Staging of Head and Neck Squamous Cell Carcinoma," *Clinical Cancer Research*, vol. 28, no. 20, pp. 4425–4434, Oct. 2022. [Online]. Available: https://doi.org/10.1158/1078-0432.CCR-22-0094

[3] J. Sun, Z. Huangfu, J. Yang, G. Wang, K. Hu, M. Gao, and Z. Zhong, "Imaging-guided targeted radionuclide tumor therapy: From concept to clinical translation," *Advanced Drug Delivery Reviews*, vol. 190, p. 114538, Nov. 2022. [Online]. Available: https://www.sciencedirect.com/science/article/pii/S0169409X22004288

[4] S. C. George and E. J. J. Samuel, "Developments in 177Lu-based radiopharmaceutical therapy and dosimetry," *Frontiers in Chemistry*, vol. 11, 2023. [Online]. Available: https://www.frontiersin.org/articles/10.3389/fchem.2023.1218670

[5] M. Vyas and S. W. Leslie, "Nuclear Medicine Applications in Prostate

Cancer," in *StatPearls*. Treasure Island (FL): StatPearls Publishing, 2023. [Online]. Available: http://www.ncbi.nlm.nih.gov/books/NBK592382/

[6] J.-K. Yoon, B.-N. Park, E.-K. Ryu, Y.-S. An, and S.-J. Lee, "Current Perspectives on 89Zr-PET Imaging," *International Journal of Molecular Sciences*, vol. 21, no. 12, p. 4309, Jan. 2020, number: 12 Publisher: Multidisciplinary Digital Publishing Institute. [Online]. Available: https://www.mdpi.com/1422-0067/21/12/4309

[7] J. A. Sorenson and M. E. Phelps, *Physics in Nuclear Medicine*. Saunders, 2003.

[8] G. F. Knoll, *Radiation detection and measurement*, 3rd ed. New York: Wiley, 2000.

[9] N. R. C. U. a. I. o. M. U. C. o. t. M. a. P. o. E. D. B. Imaging, "Single Photon Emission Computed Tomography," in *Mathematics and Physics of Emerging Biomedical Imaging*. National Academies Press (US), 1996. [Online]. Available: https://www.ncbi.nlm.nih.gov/books/NBK232492/

[10] V. Schonfelder, A. Hirner, and K. Schneider, "A telescope for soft gamma ray astronomy," *Nuclear Instruments and Methods*, vol. 107, no. 2, pp. 385–394, Mar. 1973. [Online]. Available: https://www.sciencedirect.com/science/article/pii/0029554X73902577

[11] M. Singh, "An electronically collimated gamma camera for single photon emission computed tomography. Part I: Theoretical considerations and design criteria," *Med Phys*, vol. 10, no. 4, pp. 421–427, 1983.

[12] M. Singh and D. Doria, "An electronically collimated gamma camera for single photon emission computed tomography. Part II:

Image reconstruction and preliminary experimental measurements," *Medical Physics*, vol. 10, no. 4, pp. 428–435, 1983, _eprint: https://onlinelibrary.wiley.com/doi/pdf/10.1118/1.595314. [Online]. Available: https://onlinelibrary.wiley.com/doi/abs/10.1118/1.595314

[13] M. Singh, "An electronically collimated gamma camera for single photon emission computed tomography. Part I: Theoretical considerations and design criteria," *Medical Physics*, vol. 10, no. 4, pp. 421–427, 1983, _eprint: https://onlinelibrary.wiley.com/doi/pdf/10.1118/1.595313. [Online]. Available: https://onlinelibrary.wiley.com/doi/abs/10.1118/1.595313

[14] M. D. Harpen, "Positronium: Review of symmetry, conserved quantities and decay for the radiological physicist," *Medical Physics*, vol. 31, no. 1, pp. 57–61, 2004, _eprint: https://onlinelibrary.wiley.com/doi/pdf/10.1118/1.1630494. [Online]. Available: https://onlinelibrary.wiley.com/doi/abs/10.1118/1.1630494

[15] F. J. Beekman, C. Kamphuis, S. Koustoulidou, R. M. Ramakers, and M. C. Goorden, "Positron range-free and multi-isotope tomography of positron emitters," *Phys. Med. Biol.*, vol. 66, no. 6, p. 065011, Mar. 2021, publisher: IOP Publishing. [Online]. Available: https://dx.doi.org/10.1088/1361-6560/abe5fc

[16] E. C. Pratt *et al.*, "Simultaneous quantitative imaging of two PET radiotracers via the detection of positron - electron annihilation and prompt gamma emissions," *Nat. Biomed. Eng*, vol. 7, no. 8, pp. 1028–1039, Aug. 2023, number: 8 Publisher: Nature Publishing Group. [Online]. Available: https://www.nature.com/articles/s41551-023-01060-y

[17] P. Moskal *et al.*, "Feasibility study of the positronium imaging

with the J-PET tomograph," *Phys. Med. Biol.*, vol. 64, no. 5, p. 055017, Mar. 2019, publisher: IOP Publishing. [Online]. Available: https://dx.doi.org/10.1088/1361-6560/aafe20

[18] L. M. Carter, A. L. Kesner, E. C. Pratt, V. A. Sanders, A. V. F. Massicano, C. S. Cutler, S. E. Lapi, and J. S. Lewis, "The Impact of Positron Range on PET Resolution, Evaluated with Phantoms and PHITS Monte Carlo Simulations for Conventional and Non-conventional Radionuclides," *Molecular imaging and biology*, vol. 22, no. 1, p. 73, Feb. 2020, publisher: NIH Public Access. [Online]. Available: https://www.ncbi.nlm.nih.gov/pmc/articles/PMC6805144/

[19] "Lutetium-177 PSMA Therapy for Prostate Cancer (Pluvicto)." [Online]. Available: https://www.uchicagomedicine.org/cancer/types-treatments/prostate-cancer/treatment/lutetium-177-psma-therapy-for-prostate-cancer

[20] H. Tashima, E. Yoshida, H. Wakizaka, M. Takahashi, K. Nagatsu, A. B. Tsuji, K. Kamada, K. Parodi, and T. Yamaya, "3D Compton image reconstruction method for whole gamma imaging," *Phys. Med. Biol.*, vol. 65, no. 22, p. 225038, Nov. 2020, publisher: IOP Publishing. [Online]. Available: https://dx.doi.org/10.1088/1361-6560/abb92e

[21] D. Giovagnoli *et al.*, "A Pseudo-TOF Image Reconstruction Approach for Three-Gamma Small Animal Imaging," *IEEE Transactions on Radiation and Plasma Medical Sciences*, vol. 5, no. 6, pp. 826–834, Nov. 2021, conference Name: IEEE Transactions on Radiation and Plasma Medical Sciences. [Online]. Available: https://ieeexplore.ieee.org/document/9309316

[22] B. Jasinska *et al.*, "Human Tissue Investigations Using PALS Technique - Free Radicals Influence," *Acta Phys. Pol. A*, vol. 132, no. 5, pp. 1556–1559,

Nov. 2017. [Online]. Available: http://przyrbwn.icm.edu.pl/APP/PDF/132/app132z5p26.pdf

[23] ——, "Human Tissues Investigation Using PALS Technique," *Acta Phys. Pol. B*, vol. 48, no. 10, p. 1737, 2017. [Online]. Available: http://www.actaphys.uj.edu.pl/findarticle?series=Reg&vol=48&page=1737

[24] Y. Wang, R. Herbst, and S. Abbaszadeh, "Development and characterization of modular readout design for two-panel head-and-neck dedicated pet system based on czt detectors," *IEEE Transactions on Radiation and Plasma Medical Sciences*, vol. 6, no. 5, pp. 517–521, 2022.

[25] M. Li, B. Yockey, and S. Abbaszadeh, "Design study of a dedicated head and neck cancer pet system," *IEEE Transactions on Radiation and Plasma Medical Sciences*, vol. 4, no. 4, pp. 489–497, 2020.

[26] F. Natterer, "1. Computerized Tomography," in *The Mathematics of Computerized Tomography*, ser. Classics in Applied Mathematics. Society for Industrial and Applied Mathematics, Jan. 2001, pp. 1–8. [Online]. Available: https://epubs.siam.org/doi/10.1137/1.9780898719284.ch1

[27] F. Terzioglu, "Exact inversion of an integral transform arising in Compton camera imaging," *J Med Imaging (Bellingham)*, vol. 7, no. 3, p. 032504, May 2020. [Online]. Available: https://www.ncbi.nlm.nih.gov/pmc/articles/PMC7064017/

[28] M. Cree and P. Bones, "Towards direct reconstruction from a gamma camera based on Compton scattering," *IEEE Transactions on Medical Imaging*, vol. 13, no. 2, pp. 398–407, Jun. 1994, conference Name:

IEEE Transactions on Medical Imaging. [Online]. Available: https://ieeexplore.ieee.org/document/293932

[29] F. Terzioglu, P. Kuchment, and L. Kunyansky, "Compton camera imaging and the cone transform: a brief overview*," *Inverse Problems*, vol. 34, no. 5, p. 054002, Apr. 2018, publisher: IOP Publishing. [Online]. Available: https://dx.doi.org/10.1088/1361-6420/aab0ab

[30] H. K. Tuy, "An Inversion Formula for Cone-Beam Reconstruction," *SIAM J. Appl. Math.*, vol. 43, no. 3, pp. 546–552, Jun. 1983, publisher: Society for Industrial and Applied Mathematics. [Online]. Available: https://epubs.siam.org/doi/10.1137/0143035

[31] E. Levitan and G. T. Herman, "A maximum a posteriori probability expectation maximization algorithm for image reconstruction in emission tomography," *IEEE Transactions on Medical Imaging*, vol. 6, no. 3, pp. 185–192, 1987.

[32] L. A. Shepp and Y. Vardi, "Maximum Likelihood Reconstruction for Emission Tomography," *IEEE Transactions on Medical Imaging*, vol. 1, no. 2, pp. 113–122, Oct. 1982, conference Name: IEEE Transactions on Medical Imaging.

[33] L. Parra and H. Barrett, "List-mode likelihood: EM algorithm and image quality estimation demonstrated on 2-D PET," *IEEE Transactions on Medical Imaging*, vol. 17, no. 2, pp. 228–235, Apr. 1998, conference Name: IEEE Transactions on Medical Imaging.

[34] D. Sarrut *et al.*, "The OpenGATE ecosystem for Monte Carlo simulation in medical physics," *Phys. Med. Biol.*, vol. 67, no. 18, p. 184001,

Sep. 2022, publisher: IOP Publishing. [Online]. Available: https://dx.doi.org/10.1088/1361-6560/ac8c83

[35] S. Agostinelli *et al.*, "Geant4 - a simulation toolkit," *Nuclear Instruments and Methods in Physics Research Section A: Accelerators, Spectrometers, Detectors and Associated Equipment*, vol. 506, no. 3, pp. 250–303, Jul. 2003. [Online]. Available: https://www.sciencedirect.com/science/article/pii/S0168900203013688

[36] Y. Wang, R. Herbst, and S. Abbaszadeh, "Development and Characterization of Modular Readout Design for Two-Panel Head-and-Neck Dedicated PET System Based on CZT Detectors," *IEEE Transactions on Radiation and Plasma Medical Sciences*, vol. 6, no. 5, pp. 517–521, May 2022, conference Name: IEEE Transactions on Radiation and Plasma Medical Sciences. [Online]. Available: https://ieeexplore.ieee.org/document/9534780

[37] X. Lojacono, "Image reconstruction for Compton camera with application to hadrontherapy," phdthesis, INSA de Lyon, Nov. 2013. [Online]. Available: https://theses.hal.science/tel-01081066

[38] D. Xu and Z. He, "Gamma-ray energy-imaging integrated spectral deconvolution," *Nuclear Instruments and Methods in Physics Research Section A: Accelerators, Spectrometers, Detectors and Associated Equipment*, vol. 574, no. 1, pp. 98–109, Apr. 2007. [Online]. Available: https://www.sciencedirect.com/science/article/pii/S0168900207002549

[39] Y. Feng, J. M. LÃľtang, D. Sarrut, and V. Maxim, "Influence of Doppler broadening model accuracy in Compton camera list-mode MLEM reconstruction," *Inverse Problems in Science and Engineering*,

vol. 29, no. 13, pp. 3509–3529, Dec. 2021. [Online]. Available: https://www.tandfonline.com/doi/full/10.1080/17415977.2021.2011863

[40] A. Zoglauer and G. Kanbach, "Doppler broadening as a lower limit to the angular resolution of next-generation Compton telescopes," in *X-Ray and Gamma-Ray Telescopes and Instruments for Astronomy*, vol. 4851. SPIE, Mar. 2003, pp. 1302–1309. [Online]. Available: https://www.spiedigitallibrary.org/conference-proceedings-of-spie/4851/0000/Doppler-broadening-as-a-lower-limit-to-the-angular-resolution/10.1117/12.461177.full

[41] H. Zhang, Y. Wang, J. Qi, and S. Abbaszadeh, "Penalized maximum-likelihood reconstruction for improving limited-angle artifacts in a dedicated head and neck PET system," *Phys. Med. Biol.*, vol. 65, no. 16, p. 165016, Aug. 2020, publisher: IOP Publishing. [Online]. Available: https://dx.doi.org/10.1088/1361-6560/ab8c92

[42] V. Maxim, "Enhancement of Compton camera images reconstructed by inversion of a conical Radon transform," *Inverse Problems*, vol. 35, no. 1, p. 014001, Jan. 2019. [Online]. Available: https://iopscience.iop.org/article/10.1088/1361-6420/aaecdb

[43] Y. Feng, A. Etxebeste, D. Sarrut, J. M. Letang, and V. Maxim, "3-D Reconstruction Benchmark of a Compton Camera Against a Parallel-Hole Gamma Camera on Ideal Data," *IEEE Trans. Radiat. Plasma Med. Sci.*, vol. 4, no. 4, pp. 479–488, Jul. 2020. [Online]. Available: https://ieeexplore.ieee.org/document/8913523/

[44] D. P. Watts, J. Bordes, J. R. Brown, A. Cherlin, R. Newton, J. Allison, M. Bashkanov, N. Efthimiou, and N. A. Zachariou, "Photon

quantum entanglement in the MeV regime and its application in PET imaging," *Nat Commun*, vol. 12, no. 1, p. 2646, May 2021, number: 1 Publisher: Nature Publishing Group. [Online]. Available: https://www.nature.com/articles/s41467-021-22907-5